

1 **Discovery of pan-ErbB inhibitors protecting from SARS-CoV-2 replication, inflammation,**
2 **and lung injury by a drug repurposing screen**
3
4

5 Sirle Saul^{1, 12}, Marwah Karim^{1, 12}, Pei-Tzu Huang^{1, 13}, Luca Ghita^{1, 13}, Winston Chiu², Sathish
6 Kumar¹, Nishank Bhalla³, Pieter Leyssen², Courtney A. Cohen⁴, Kathleen Huie⁴, Courtney
7 Tindle^{5, 6}, Mamdouh Sibai⁷, Benjamin A. Pinsky^{7, 1}, Soumita Das^{6, 8}, Pradipta Ghosh^{5, 6, 9}, John
8 M. Dye⁴, David E. Solow-Cordero¹⁰, Jing Jin¹¹, Dirk Jochmans², Johan Neyts², Aarthi
9 Narayanan³, Steven De Jonghe², and Shirir Einav^{1, *}
10

11 ¹Department of Medicine, Division of Infectious Diseases and Geographic Medicine, and
12 Department of Microbiology and Immunology, Stanford University, CA, USA

13 ² KU Leuven, Department of Microbiology, Immunology and Transplantation, Rega Institute for
14 Medical Research, Laboratory of Virology and Chemotherapy, Belgium

15 ³National Center for Biodefence and Infectious Disease, Biomedical Research Laboratory,
16 School of Systems Biology, George Mason University, Manassas, VA, USA.

17 ⁴US Army Medical Research Institute of Infectious Diseases, Viral Immunology Branch, Fort
18 Detrick, Maryland

19 ⁵Department of Cellular and Molecular Medicine, University of California San Diego

20 ⁶ HUMANOID CoRE, University of California San Diego.

21 ⁷Department of Pathology, Stanford University School of Medicine, Stanford, California, USA

22 ⁸Department of Pathology, University of California San Diego

23 ⁹Department of Medicine, University of California San Diego

24 ¹⁰High-Throughput Bioscience Center, Department of Chemical and Systems Biology, Stanford
25 University, CA

26 ¹¹ Vitalant Research Institute, San Francisco, CA, USA

27
28 * Corresponding author and lead contact: seinav@stanford.edu
29

30 ¹²These authors contributed equally

31 ¹³These authors also contributed equally
32
33
34
35
36
37
38
39
40
41
42
43
44

45 **Abstract**

46

47 Effective therapies are needed to combat emerging viruses. Seventeen candidates that rescue
48 cells from SARS-CoV-2-induced lethality and target diverse functions emerged in a screen of
49 4,413 compounds. Among the hits was lapatinib, an approved inhibitor of the ErbB family of
50 receptor tyrosine kinases. Lapatinib and other pan-ErbB inhibitors suppress replication of
51 SARS-CoV-2 and unrelated viruses with a high barrier to resistance. ErbB4, but not lapatinib's
52 cancer targets ErbB1 and ErbB2, is required for SARS-CoV-2 entry and encephalitis alphavirus
53 infection and is a molecular target mediating lapatinib's antiviral effect. In human lung
54 organoids, lapatinib protects from SARS-CoV-2-induced activation of pathways implicated in
55 non-infectious acute lung injury and fibrosis downstream of ErbBs (p38-MAPK, MEK/ERK, and
56 AKT/mTOR), pro-inflammatory cytokine production, and epithelial barrier injury. These findings
57 reveal regulation of viral infection, inflammation, and lung injury via ErbBs and propose
58 approved candidates to counteract these effects with implications for pandemic coronaviruses
59 and unrelated viruses.

60

61

62

63

64

65

66

67

68

69

70

71

72

73

74

75

76

77

78

79 Introduction

80

81 Severe acute respiratory syndrome coronavirus-2 (SARS-CoV-2) has spread globally, resulting
82 in the Coronavirus Disease 2019 (COVID-19) pandemic. While largely asymptomatic or mild, in
83 3-21% of symptomatic patients, COVID-19 progresses to acute lung injury (ALI) and acute
84 respiratory distress syndrome (ARDS) associated with a 5-20% 28-day death rate in face of
85 standard of care¹⁻³. Survivors of severe COVID-19 are also at risk of developing lung fibrosis⁴.

86

87 The development of countermeasures that reduce COVID-19 morbidity and mortality via off-
88 label use of existing drugs has been an area of much global research. Unbiased screens have
89 discovered repurposing drug candidates for the treatment of COVID-19^{5,6,7,8}, several of which
90 are still studied clinically. Nevertheless, to date the reported clinical benefit in reducing
91 complication and mortality rates has been overall limited⁹. Moreover, no single agent capable of
92 suppressing viral infection, inflammation and tissue injury has been identified. There is thus an
93 urgent need for more effective approaches to prevent the acute and long-term complications
94 associated with COVID-19 and ideally provide readiness for future outbreaks.

95

96 To address these gaps, we conducted a high-throughput screen of existing compounds for
97 agents that rescue mammalian cells from SARS-CoV-2-induced lethality. Among the promising
98 hits were inhibitors of members of the ErbB family of receptor tyrosine kinases, including
99 lapatinib, an approved anticancer drug. Here, we reveal regulation of SARS-CoV-2 infection and
100 pathogenesis via ErbBs and characterize the therapeutic potential and mechanism of action of
101 lapatinib and other pan-ErbB inhibitors as a candidate broad-spectrum antiviral, anti-
102 inflammatory and tissue protective strategy, with implications for future pandemic coronaviruses
103 and beyond.

104

105 Results

106

107 High-throughput screening (HTS) for compounds that counteract SARS-CoV-2-induced 108 lethality

109

110 We assembled a collection of 4,413 bioactive investigational and FDA approved compounds
111 derived from four commercially available libraries and a self-assembled set of 13 kinase
112 inhibitors (**Fig. 1a and Extended Data Fig. 1a**). This collection was screened in two
113 independent experiments for inhibition of lethality induced by SARS-CoV-2 (isolate: Belgium-
114 GHB-03021) in Vero E6 cells constitutively expressing an enhanced green fluorescent protein
115 (eGFP) via a high-throughput assay¹⁰ (**Fig. 1b**). The average percent fluorescent area for
116 control wells included in each plate was 102.9±5% for uninfected cells (cell control), 0.1±0.2%
117 for infected untreated cells (virus control), and 0.0±0.164% for infected cells treated with DMSO
118 (**Fig. 1c**). The Z' and RZ' values of each of the 29 screen plates, calculated based on the virus
119 control and cell control wells, were greater than 0.78 (**Extended Data Fig. 1b**). The signal-to-
120 background (S/B) value, representing the ratio of the median value of the raw data between the
121 virus control and the cell control, was greater than 120 (**Extended Data Fig. 1b**). The two
122 replicate screens demonstrated good correlation (r= 0.76) (**Extended Data Fig. 1c**). Remdesivir

123 and its major metabolite, GS-441524, used as positive controls, demonstrated dose-dependent
124 anti-SARS-CoV-2 activity in this assay (**Extended Data Fig. 1d**). Overall, these data indicate
125 that this antiviral assay is robust for HTS and is specific.

126
127 We set a percent area of greater than 15 in at least one of the two screens as the cutoff for
128 positive hits (**Fig. 1c and Extended Data Fig. 2a**). 40 compounds from the commercial libraries
129 and two from the kinase inhibitor set met this criterion. Nelfinavir and salinomycin, but not
130 ivermectin, previously demonstrating anti-SARS-CoV-2 activity^{9,11}, emerged by our more
131 stringent assay. Eighteen of the 42 hits were prioritized based on PubChem data documenting
132 lower promiscuity and toxicity or activity against other viruses (**Fig. 1a**).

133 134 **Dose-dependent effect of hits in an orthogonal antiviral assay**

135
136 The 18 prioritized compounds were then studied for their effect on SARS-CoV-2 infection and
137 cellular viability in Vero cells infected with a distinct viral isolate (2019-nCoV/USA-WA1/2020)
138 via plaque and alamarBlue assays, respectively. Seven compounds showed potent dose-
139 dependent antiviral activity with EC₅₀ (half-maximal effective concentration) <0.7 μM, CC₅₀ (half-
140 maximal cellular cytotoxicity) >20 μM, and selectivity indices (SI, CC₅₀ to EC₅₀ ratio) >29 (**Fig.**
141 **1d, 1e and Extended Data Fig. 2b**). Six compounds showed moderate antiviral activity beyond
142 toxicity with EC₅₀ values of 1.2-4.3 μM, CC₅₀>20 μM, and SI>5.1. Four compounds effectively
143 suppressed SARS-CoV-2 infection without apparent toxicity at the tested concentrations, albeit
144 with higher EC₅₀ values. Salbutamol showed no anti-SARS-CoV-2 activity (**Fig. 1d and**
145 **Extended Data Fig. 2b**). In total, 17 hits demonstrated antiviral effect beyond toxicity, and 12 of
146 these were effective at sub to low micromolar concentrations. These compounds target diverse
147 cellular factors and functions (**Fig. 1f**). Two of the hits are known to target ErbBs: lapatinib
148 (approved anticancer)¹² and tyrphostin AG 879 (experimental)¹³. Inhibitors of NUMB-associated
149 kinases (NAK), heat shock protein 90 (HSP90) and ion transport across cell membranes were
150 also among the hits. Five of the compounds have been previously approved for other indications
151 and seven are natural products (**Fig. 1f**).

152 153 **Broad-spectrum antiviral activity of hits**

154
155 In parallel, we studied the effect of the 18 emerging hits on replication of two unrelated RNA
156 viruses, the alphavirus Venezuelan equine encephalitis virus vaccine strain (VEEV (TC-83)),
157 and the flavivirus, dengue (DENV2) in human astrocytes (U-87 MG) and hepatoma (Huh7) cells,
158 respectively, both via luciferase assays. Lycorine, calcimycin, monensin, azaserine, gedunin,
159 and the kinase inhibitors lapatinib and tyrphostin AG 879 dose-dependently inhibited replication
160 of VEEV (TC-83) and DENV2 (**Extended Data Fig. 3**). Several compounds showed more
161 potent anti-VEEV (TC-83) and DENV2 activity than anti-SARS-CoV-2 activity, and others
162 showed variable activity against one or two of these viruses. Salbutamol demonstrated minimal
163 to no activity against all three viruses (**Extended Data Fig. 2b and 3**).

164 165 **Lapatinib has a broad-spectrum antiviral activity and a high genetic barrier to resistance**

166

167 We focused on defining the therapeutic potential of lapatinib, an already approved pan-ErbB
168 inhibitor that emerged in the screen (**Fig. 2a**). Lapatinib dose-dependently inhibited replication
169 of SARS-CoV-2 (USA-WA1/2020 strain) in both Calu-3 (human lung epithelial) and Vero cells
170 measured via plaque assays ($EC_{50}=0.5-0.7 \mu\text{M}$, $CC_{50}>20 \mu\text{M}$) (**Fig. 2b and 1e**). Moreover,
171 lapatinib demonstrated a dose-dependent rescue of Vero-eGFP cells from SARS-CoV-2-
172 induced lethality (Belgium-GHB-03021 strain) (**Fig. 2c, d**).

173
174 Lapatinib dose-dependently inhibited infections of both vaccine (TC-83) and wild type (WT)
175 (Trinidad donkey, TrD) VEEV measured by plaque assays in U-87 MG cells ($EC_{50}=0.8 \mu\text{M}$, CC_{50}
176 $>20 \mu\text{M}$) (**Fig. 2e, f**). Similarly, it dose-dependently inhibited the replication of DENV2 ($EC_{50}=1.8$
177 μM) measured via plaque assays, and the filoviruses Ebola (EBOV) ($EC_{50}=2.5 \mu\text{M}$) and Marburg
178 viruses (MARV) ($EC_{50}=1.9 \mu\text{M}$) measured via microneutralization assays in Huh7 cells, albeit
179 lower CC_{50} values were measured in infected Huh7 cells ($10.2-10.5 \mu\text{M}$) relative to the other cell
180 lines (**Fig. 2g-i**).

181
182 To determine whether viruses can escape treatment with lapatinib, we focused on VEEV (TC-
183 83) since it replicates robustly in cultured cells, has a short life cycle, and its handling does not
184 require BSL3 containment. VEEV was passaged in U-87 MG cells in the presence of lapatinib or
185 the nonstructural protein 2 (nsP2) inhibitor ML336¹⁴ and viral titers were measured in culture
186 supernatants by plaque assays. By passage 3, VEEV overcame inhibition by ML336. In
187 contrast, VEEV remained suppressed for 10 passages under lapatinib treatment without
188 phenotypic resistance (**Fig. 2j**). Virus obtained from culture supernatants at passage 10 under
189 lapatinib or DMSO treatment remained susceptible to lapatinib (**Fig. 2k**). Conversely, virus
190 obtained at passage 10 under ML336, but not DMSO, treatment, lost its susceptibility to ML336,
191 with the emergence of a resistance mutation in nsP2 (Y102C in TC-83) (**Fig. 2l**).

192
193 These results point to lapatinib as a potential broad-spectrum antiviral agent with a higher
194 relative barrier to resistance than a direct-acting antiviral.

195

196 **Lapatinib inhibits SARS-CoV-2 entry**

197

198 To understand lapatinib's target(s) and mechanism of antiviral action, we first tested the
199 hypothesis that by targeting receptor tyrosine kinases, it inhibits the entry of vesicular stomatitis
200 virus encapsidated RNA pseudotyped with the SARS-CoV-2 spike glycoprotein (rVSV-SARS-
201 CoV-2-S). Treatment of Calu-3 and Vero cells with lapatinib dose-dependently suppressed
202 rVSV-SARS-CoV-2-S infection measured by luciferase assays without impacting cell viability
203 ($EC_{50}=2.6-3.2 \mu\text{M}$, $CC_{50} >20 \mu\text{M}$) (**Fig. 3a, b and Extended Data Fig. 4a**). Moreover, lapatinib
204 suppressed the level of intracellular viral RNA at 3 hours post-infection with a high rVSV-SARS-
205 CoV-2-S inoculum measured via RT-qPCR (**Fig. 3a, c**). These results highlight a defect in the
206 entry step, yet, it is possible that lapatinib inhibits additional stages of the SARS-CoV-2 life
207 cycle.

208

209 **ErbB4, but not other lapatinib's targets, is essential for SARS-CoV-2 entry and VEEV (TC- 210 83) infection**

211
212 The ErbB family is composed of four members (ErbB1-4), of which three are catalytically active:
213 ErbB1, 2, and 4¹⁵. Lapatinib's cancer targets are ErbB1 (EGFR) (IC₅₀=5.3 nM) and ErbB2
214 (HER2) (IC₅₀=35 nM)¹². Yet, its kinome (ID:20107) reveals potent binding to 5 additional kinases
215 (ErbB4, RAF1, RIPK2, STK10, and MAP2K5), with an overall excellent selectivity. To define
216 which of these 7 molecular targets mediate(s) the observed antiviral effect of lapatinib, we
217 studied the effects of siRNA-mediated depletion of these kinases on rVSV-SARS-CoV-2-S and
218 VEEV (TC-83) infections. Depletion of ErbBs by siRNA pools was confirmed (**Extended Data**
219 **Fig. 4b, c**). ErbB4 depletion suppressed rVSV-SARS-CoV-2-S infection in Vero cells by 73%
220 (**Fig. 3d, e**) and VEEV (TC-83) infection in U-87 MG cells by 76% relative to non-targeting (NT)
221 controls (**Extended Data Fig. 4d, e**). RIPK2 depletion mildly reduced VEEV infection, but not
222 rVSV-SARS-CoV-2-S infection (**Fig. 3e and Extended Data Fig. 4e**). Depletion of the
223 remaining 5 targets, including ErbB1 and ErbB2, had no effect on infection of both viruses.
224 None of these siRNA pools impacted cellular viability (**Fig. 3e and Extended Data Fig. 4e**).
225

226 Silencing ErbB4 expression by two siRNAs targeting distinct regions suppressed rVSV-SARS-
227 CoV-2-S infection by 80-85% and VEEV (T-83) infection by 60-95% relative to siNT (**Fig. 3f, g**
228 **and Extended Data Fig. 4f, g**). Moreover, these siErbB4s suppressed WT SARS-CoV-2
229 infection by 78-97% and SARS-CoV-2 entry by 50-80% relative to siNT (**Fig. 2d, f, h, i**). ErbB4
230 depletion did not impact cell viability (**Fig. 3e, g, h and Extended Data Fig. 4e, g**) and largely
231 correlated with the observed phenotype. These findings confirm a role for ErbB4 in viral entry; a
232 step of the viral life cycle that is also inhibited by lapatinib.
233

234 Lapatinib was shown to bind the ATP binding site of ErbB4 in a comparable manner to ErbB1
235 and ErbB2 binding¹⁶. We measured an IC₅₀ of 28 nM on ErbB4 in a cell-free assay (vs. IC₅₀=430
236 nM reported with a different peptide¹⁷) and confirmed anti-ErbB2 activity (**Extended Data Fig.**
237 **4h**).
238

239 To further probe the requirement for ErbBs in SARS-CoV-2 infection, we evaluated the antiviral
240 effect of chemically distinct compounds with anti-ErbB activity. Tyrphostin AG 879¹³, an
241 experimental compound that emerged in the HTS, dose-dependently inhibited SARS-CoV-2 and
242 rVSV-SARS-CoV-2-S infections in Calu-3 cells (EC₅₀=0.5-1.1 μM, CC₅₀>20 μM (**Fig. 3j and**
243 **Extended Data Fig. 4i**). Yet, its activity on ErbB2 and 4 could not be confirmed (**Extended**
244 **Data Fig. 4h**), suggesting that another target may mediate its antiviral activity. While not
245 included in the original screen, ibrutinib (**Fig. 3k**), an approved anticancer Bruton's tyrosine
246 kinase (BTK) inhibitor, and sapitinib (investigational) (**Fig. 3l**), with potent pan-ErbB activity^{12,18},
247 suppressed both SARS-CoV-2 and rVSV-SARS-CoV-2-S infections, with EC₅₀ values at sub to
248 low micromolar range and CC₅₀>20 μM (**Fig. 3k-m and Extended Data Fig. 4h-j**).
249

250 Collectively, these results provide evidence that ErbB4, but not ErbB1 or 2, is required for
251 SARS-CoV-2 entry and VEEV (TC-83) infection, thereby validating it as a druggable antiviral
252 target. Its role as an entry co-factor, a step of the life cycle that is inhibited by lapatinib, supports
253 a hypothesis that inhibition of ErbB4 mediates the antiviral effect of lapatinib.
254

255 **ErbB4 is a molecular target mediating the antiviral effect of lapatinib**

256

257 To determine whether lapatinib exerts its antiviral effect by inhibiting phosphorylation of ErbBs,
258 lysates derived from SARS-CoV-2-infected Calu-3 cells treated with lapatinib or DMSO were
259 subject to Western blot analysis. Lapatinib treatment dose-dependently suppressed the ratio of
260 phosphorylated to total ErbB1, 2, and 4 levels at 24 hours post-infection with EC₅₀ values lower
261 than 0.1 μM that correlated with reduced expression of the SARS-CoV-2 nucleocapsid protein
262 (**Fig. 4a, b**). Similar findings were observed at 1.5 hour post-infection (**Extended Data Fig. 5**).
263 These results provide evidence that drug exposure and the antiviral effect of lapatinib are
264 correlated with functional inhibition of ErbBs' activity.

265

266 To confirm that inhibition of ErbB4 is a mechanism underlying the antiviral effect of lapatinib, we
267 conducted gain-of-function assays. Ectopic expression of WT ErbB4, but not catalytically
268 inactive ErbB4 mutant harboring a lysine to arginine substitution in position 751 (K751R) or
269 control plasmid, either completely or partially reversed the antiviral effect of lapatinib on rVSV-
270 SARS-CoV-2-S infection (**Fig. 4c-e and Extended Data Fig. 6a**). Similarly, WT, but not the
271 ErbB4 mutant, reversed the effect of lapatinib on VEEV (TC-83) infection (**Extended Data Fig.**
272 **6b-e**). These results validate ErbB4 as a key mediator of the antiviral effect of lapatinib and
273 indicate that its enzymatic activity is required for viral infection.

274

275 **Lapatinib inhibits SARS-CoV-2-induced activation of ErbB-regulated inflammatory and**
276 **tissue injury signals**

277

278 In non-infectious ALI and ARDS, animal and human data indicate that ErbB1 and 2 are key
279 regulators of inflammation and tissue injury via activation of the p38 MAPK, AKT/mTOR and
280 Ras/RAF/MEK/ERK pathways^{15,19-27}. To test the hypothesis that these pathways are activated in
281 SARS-CoV-2 infection and suppressed by the pan-ErbB inhibitory effect of lapatinib, we
282 measured their activation in Calu-3 cells upon SARS-CoV-2 infection and/or lapatinib treatment
283 by Western blot analysis. At 1.5 and 24 hours post-infection, SARS-CoV-2 increased the ratio of
284 phosphorylated to total protein level of AKT, ERK, and/or p38 MAPK by >1.5-2.5 fold (**Fig. 4b,**
285 **f**), in agreement with reports in other cell lines^{8,28}. Lapatinib treatment dramatically inhibited
286 SARS-CoV-2-induced activation of AKT and ERK both at 1.5 and 24 hours post-infection and of
287 p38 MAPK at 24 hours post-infection (**Fig. 4b, f**).

288

289 These results provide evidence that lapatinib inhibits SARS-CoV-2-induced activation of
290 signaling pathways downstream of ErbBs, which are implicated in non-infectious ALI/ARDS.

291

292 **Lapatinib inhibits SARS-CoV-2 infection, inflammation, and tissue injury *ex vivo* in**
293 **human adult lung organoids (ALO)**

294

295 Next, we studied the effect of lapatinib treatment on SARS-CoV-2 infection in a biologically
296 relevant, validated human ALO monolayer model. Generated from adult stem cells isolated from
297 lung tissue, these organoids contain both proximal airway cells, critical for sustained viral
298 infection, and distal alveolar cells, required for mounting the overzealous host immune response

299 in fatal COVID-19²⁹ (**Fig. 5a**). Viral replication measured by plaque assays in culture
300 supernatant and nucleocapsid transcript expression measured by RT-qPCR in ALO monolayer
301 lysates both peaked at 48 hours following SARS-CoV-2 infection (**Extended Data Fig. 7a, b**),
302 and were effectively suppressed by lapatinib, with EC₅₀ values of 0.4 μM and <0.2 μM,
303 respectively, and CC₅₀ > 20 μM (**Fig. 5a-c**). Confocal immunofluorescence (IF) analysis
304 revealed a near-complete disappearance of SARS-CoV-2 nucleocapsid staining in epithelial cell
305 clusters forming alveolar-like structures and resembling AT2 cells in ALOs treated with 10 μM of
306 lapatinib relative to DMSO controls (**Fig. 5d and Extended Data Fig. 7c**).

307
308 As in Calu-3 cells, lapatinib treatment dose-dependently inhibited phosphorylation of ErbB1, 2
309 and 4, indicating an association between its antiviral effect and ErbB modulation in these ALOs
310 (**Fig. 5e**). Moreover, lapatinib treatment inhibited SARS-CoV-2-induced phosphorylation of AKT
311 and ERK, albeit not p38 MAPK, in this more complex tissue model (**Fig. 5f**).

312
313 To test the hypothesis that ErbB-regulated signaling mediates the inflammatory response to
314 SARS-CoV-2 infection, we measured cytokine levels in ALO culture supernatants upon SARS-
315 CoV-2 infection and treatment with lapatinib or DMSO. SARS-CoV-2 infection increased the
316 production of TNF-α, IL-1β and IL-6, in agreement with former reports³⁰. Lapatinib treatment
317 dose-dependently reduced the expression level of these pro-inflammatory cytokines, with levels
318 at or lower than those measured in uninfected organoids achieved at drug concentration of 0.5
319 μM (**Fig. 5g**). Concurrently, lapatinib increased the expression level of MCP-1 (**Fig. 5g**),
320 suggesting that it may augment innate immune responses³¹.

321
322 Lastly, to define the role of ErbB signaling in SARS-CoV-2-induced lung injury, we analyzed the
323 effect of lapatinib on the integrity of tight junction formation in ALOs via confocal IF analysis.
324 Lapatinib was added to ALO monolayers 4 hours post-infection, to minimize its direct antiviral
325 effect. Claudin 7 staining of uninfected ALOs revealed a continuous membranous pattern (**Fig.**
326 **5h, i and Extended Data Fig. 7d**). Thirty-six hours following SARS-CoV-2 infection and DMSO
327 treatment, claudin 7 stained as speckles or short segments that often appeared in the
328 cytoplasmic region. This finding was accompanied by cell separation and destruction of the
329 alveolar-like architecture. In contrast, ALOs treated with 10 μM of lapatinib exhibited intact
330 claudin 7 morphology and subcellular distribution and preserved architecture of the alveolar-like
331 structure, comparable to uninfected controls (**Fig. 5h, i and Extended Data Fig. 7d**).

332
333 Together, these findings reveal regulation of SARS-CoV-2 infection, inflammation and epithelial
334 barrier injury via ErbBs and provide a proof of concept for the utility of pan-ErbB inhibitors in
335 suppressing these processes in a model that recapitulates COVID-19 pathology.

336 337 **Discussion**

338
339 Seventeen compounds targeting a diverse repertoire of functions that suppress SARS-CoV-2
340 infection and protect cells from its lethality, some with a broad-spectrum antiviral activity,
341 emerged from our HTS. We integrated virology, biochemistry, genetic, immunological, and
342 pharmacological approaches with a unique human lung organoid model to define the

343 therapeutic potential of lapatinib, an approved pan-ErbB inhibitor, as an antiviral agent and
344 characterize its mechanism of action.

345
346 Our findings point to lapatinib and other pan-ErbB inhibitors as a class of broad-spectrum
347 antiviral agents with a higher relative barrier to resistance than a classical direct-acting antiviral.
348 Most antiviral strategies target viral enzymes, thereby typically providing a “one drug, one bug”
349 approach that is prone to the emergence of viral resistance and is not easily scalable to meet
350 the large unmet need^{9,32}. While polymerase inhibitors, such as remdesivir and favipiravir, can
351 suppress replication of unrelated viruses, the reported clinical benefit to date has been mild to
352 moderate^{2,9}. Lapatinib has recently emerged in an independent screen for anti-SARS-CoV-2
353 compounds in human lung fibroblasts³³ and in an *in silico* screen³⁴, but otherwise has not been
354 studied for its antiviral activity or mechanism of antiviral action.

355
356 Using lapatinib as a pharmacological tool, we discovered ErbB4, the least studied ErbB, as a
357 candidate antiviral target. Unlike other ErbBs, to the best of our knowledge, ErbB4 has not been
358 previously implicated in the life cycle of a virus. Its precise role in viral entry, via fusion at the
359 plasma membrane and/or endocytosis, remains to be elucidated. While writing this manuscript,
360 ErbB4 was identified as a candidate interactor of the SARS-CoV-2 3C-like protease via an *in*
361 *silico* approach³⁵, suggesting that it may also mediate later stages in the SARS-CoV-2 life cycle.

362
363 We provide multiple lines of evidence to support modulation of ErbB4 activity as an important
364 mechanism of antiviral action of lapatinib. Lapatinib inhibits SARS-CoV-2 entry, analogous to
365 the phenotype seen with RNAi-mediated ErbB4 suppression. Lapatinib’s antiviral activity
366 correlates with reduced phospho-ErbB4 levels, and WT, but not a kinase dead ErbB4 mutant,
367 reverses its antiviral effect against both SARS-CoV-2 entry and VEEV infection. This
368 mechanism also plays a role *ex vivo* as evidenced by the correlation of antiviral activity with
369 reduced ErbB4 phosphorylation in ALOs upon drug treatment. Inhibition of ErbB4
370 phosphorylation thus mechanistically explains, at least in part, the antiviral effect of lapatinib.

371
372 Independent of the role of ErbB4 in viral entry, we and others provide evidence that ErbBs are
373 mediators of inflammation and lung injury. Human and animal data in multiple non-infectious
374 ALI/ARDS models indicate that ErbBs are key regulators of inflammation, loss of epithelial
375 barrier function, thrombosis, vasoconstriction, and the resulting fibrosis^{15,19,25-27} - processes also
376 involved in severe COVID-19 pathogenesis⁹. Indeed, transcriptomic and phosphoproteomic
377 studies revealed that activation of ErbBs and/or their downstream pathways are among the
378 strongest detected upon infection of human cells with SARS-CoV³⁶, SARS-CoV-2^{8,28} and
379 MERS³⁷, and in mice infected with SARS-CoV³⁸, proposing roles for these pathways in pan-
380 coronaviral infections and/or pathogenesis. However, these signaling pathways have not been
381 directly linked to SARS-CoV-2-induced inflammation and lung injury. In human lung epithelium
382 and organoids, we demonstrate SARS-CoV-2-induced activation of p38 MAPK, AKT, and ERK
383 and inhibition of phosphorylation of both ErbBs and these downstream effectors by lapatinib.
384 Moreover, in human ALOs, we show that SARS-CoV-2 infection increases production of pro-
385 inflammatory cytokines and disrupts the lung epithelial barrier integrity and that lapatinib
386 treatment effectively suppresses both processes. These results establish a role for ErbB

387 pathways in SARS-CoV-2-induced inflammation and acute lung injury and propose pan-ErbB
388 inhibition as an effective means to disrupt these processes.

389
390 Based on our and the cumulative published data, we propose a model wherein ErbB4 is
391 required for SARS-CoV-2 entry, while pan-ErbB activation of downstream signaling pathways by
392 SARS-CoV-2 mediates inflammation and lung injury. By suppressing both processes, pan-ErbB
393 inhibitors, not only inhibit viral infection, but independently also reduce inflammation and tissue
394 injury (**Fig. 6**).

395
396 We predict that the anti-inflammatory and tissue protective effects of lapatinib are beyond its
397 ErbB4-mediated antiviral effect. First, these effects correlate with suppression of relevant
398 signaling pathways. Second, the tissue protective effect was observed when lapatinib was
399 added 4 hours post-infection, i.e. following the first round of viral entry. Third, lapatinib was
400 shown to reverse increased epithelium permeability in a non-infectious (IL-1 β –induced), *in vitro*
401 lung injury model²⁰. Fourth, while lapatinib has not been studied in non-infectious mouse models
402 of ALI, AG1478, an investigational ErbB1 inhibitor diminished lung alveolar permeability,
403 vascular leak, and neutrophil accumulation in the BAL in a mouse model of mechanical
404 ventilation-induced ALI³⁹.

405
406 Beyond ALI, ErbB1 and 2 are implicated in lung fibrosis²²⁻²⁴. Most relevant, ErbB1 was shown to
407 mediate SARS-CoV-induced fibrosis independently of viral titers in a STAT1-/- mouse model³⁸.
408 Notably, various ErbB1 and 2 inhibitors reduced lung fibrosis, morbidity and/or mortality in
409 bleomycin- and TGF- α induced lung fibrosis mouse models^{21,40,41}. We thus predict that lapatinib
410 may also protect from lung fibrosis.

411
412 While it remains to be experimentally proven, since ErbB1 has been shown to be required for
413 SARS-CoV infection⁴², and the pathways downstream of ErbBs are similarly upregulated in
414 SARS-CoV and MERS, we predict that this model applies to other pandemic coronaviral
415 infections.

416
417 ErbBs mediate the deleterious effects of multiple ligands implicated in ALI and lung fibrosis,
418 such as NRG-1, TGF- α , HB-EGF, and AREG, some of which have shown to play a role in
419 coronaviral infections^{19,23,24,43}. Moreover, unopposed Angiotensin (Ang) II effect activates ErbB
420 pathways⁴⁴ and was linked to increased pulmonary vascular permeability in animal models of
421 non-viral lung injury⁴⁵, whereas Ang (1–7) acts as a pan-ErbB inhibitor⁴⁶. It is thus intriguing to
422 speculate that the imbalance in the renin angiotensin system (RAS), thought to play a major role
423 in the pathogenesis of severe coronaviral infections^{9,47}, contributes to the observed activation of
424 ErbB pathways. By inhibiting ErbB activation by multiple ligands and Ang II, lapatinib should, at
425 least in theory, achieve a greater anti-inflammatory and tissue protective effect from approaches
426 that target individual components of these pathways (e.g. Ang (1-7), antibodies targeting IL-1 β ,
427 TGF- β and IL-6, and p38 MAPK inhibitors) (**Fig. 6**).

428
429 Collectively, these findings provide insight into the mechanisms underlying the antiviral, anti-
430 inflammatory, and tissue protective effects of lapatinib. The approaches being studied for

431 COVID-19 to date typically target one of these processes, but not all three. Demonstrating these
432 effects in the biologically relevant human ALO model illuminates the translatability of this
433 approach. While lapatinib has not been studied for COVID-19 treatment to date, ibrutinib has
434 shown protection from progression to severe COVID-19, albeit in a small number of patients⁴⁸.
435 This protection was thought to be mediated solely by ibrutinib's anti-inflammatory effect via its
436 cancer target, BTK. Nevertheless, beyond its anti-BTK activity, ibrutinib is a potent pan-ErbB
437 inhibitor¹² (**Fig. 3m**). Indeed, we show that like lapatinib, ibrutinib inhibits SARS-CoV-2 infection.
438 Our data provide evidence that pan-ErbB inhibition by ibrutinib mediates, at least in part, the
439 observed protective effect. Our findings thus provide insight into the mechanism of action of
440 another repurposed candidate for COVID-19 and propose additional investigational pan-ErbB
441 inhibitor candidates (e.g. sapitinib).

442
443 Repurposing existing drugs requires less capital and time and diminishes the clinical risks, as
444 such drugs have already been tested (toxicity, pharmacokinetics (PK), dosing, etc.) for their
445 primary indication⁹. Lapatinib is an oral drug that is approved globally in combination drug
446 treatments for metastatic, ErbB2-positive breast cancer. Based on the available PK data, the
447 plasma and hence lung level achieved with the approved dose of lapatinib (1500 mg once daily)
448 should be therapeutic as it is 8-10 fold higher than the EC_{50} s we measured for its anti-SARS-
449 CoV-2 effect in ALOs. Even higher lapatinib lung levels may be achieved, as suggested by the
450 predicted lung to plasma area under the curve ratio of 8.2-10⁴⁹. Although toxicity is a concern
451 when targeting host functions, lapatinib has a favorable safety profile, particularly when used as
452 a monotherapy and for short durations, as those required to treat acute infections. A summary
453 of safety considerations and drug-drug interactions is provided in Supplementary Discussion.

454
455 Other compounds targeting diverse cellular factors and functions have emerged in the HTS. A
456 summary of other compounds, their predicted targets and reported antiviral activity is provided
457 in Supplementary Discussion. One example is sunitinib, a multi-kinase inhibitor that we have
458 shown to protect mice from DENV and EBOV challenges when given in combination with
459 erlotinib by inhibiting NAK-mediated intracellular viral trafficking^{50,51}. Sunitinib was recently
460 shown to suppress pan-corona pseudotyped viral infections⁵². Compounds targeting ion
461 transport across cell membranes, HSP90 and others are additional examples. These findings
462 reveal candidate targets for anti-SARS-CoV-2 approaches.

463
464 In summary, our study validates ErbBs as druggable targets for antiviral, anti-inflammatory and
465 tissue protective approaches and proposes approved drugs with anti-pan-ErbB activity as an
466 attractive class of repurposing candidates for COVID-19 that may provide readiness for future
467 outbreaks of coronaviruses and other emerging viruses. The safety and efficacy of pan-ErbB
468 inhibition as an anti-coronaviral strategy therefore warrants clinical evaluation particularly in
469 hospitalized patients with comorbidities and/or low oxygen requirements.

470
471
472
473
474

475 **Methods:**

476

477 **Compound libraries and reagents.** The 4 commercial libraries (Microsource Spectrum library
478 of 2000 compounds, the two Biomol collections of 480 known diverse bioactive compounds with
479 defined biological activity and 640 FDA-approved drugs, and the LOPAC collection of 1280
480 pharma-developed tools and approved drugs) were available at the Stanford High-Throughput
481 Bioscience Center. Small molecule inhibitors were purchased from MedchemExpress or from
482 Cayman Chemical except for Ac-Leu-Leu-Nle-CHO (BML-P120, Enzo Life Sciences),
483 tesevatinib (A110575, Adooq Bioscience LLC), and erlotinib (E-4007, LC Laboratories).
484 Dinaciclib and ribociclib were a gift from Dr. Mardo Koivomaegi (Stanford University).

485

486 **High-throughput screening (HTS) of compound libraries.** Compounds from the libraries
487 listed above were plated in a total of 29 assay-ready 384-well plates (Greiner #7810192).
488 Dispensing of 6 μ l of the compound solutions was achieved using an automated Agilent Bravo
489 pipetting system, allowing for a final test concentration of 10 μ M (or 10-20 in the case of the self-
490 assembled kinase inhibitor collection). The HTS was based on an assay previously developed
491 to discover antiviral agents for SARS-CoV infection⁵³. Briefly, 30 μ L Vero-E6-eGFP cells were
492 added at 8000 cells/well to columns 1-24 24 hours before infection. 30 μ L assay medium was
493 added to columns 23 and 24, which were used as cell controls. Following a 20-hour incubation,
494 cells in columns 1-22 were infected with 30 μ L SARS-CoV-2 (Belgium-GHB-03021) at an MOI of
495 0.001, using an automated, no-contact liquid handler (EVO 100, Tecan) on the Caps-It robotics
496 system. Plates were then incubated for 4 days and imaged via a high content imager (Arrayscan
497 XTI, ThermoFisher) using wide-field fluorescence microscopy. eGFP signal was used as a
498 marker for survival from viral-induced lethality. The cells were excited at 485-20 nm and
499 emission was captured via a CCD camera and a BGRFRN_BGRFRN dichroic mirror and filter
500 set. A 5X objective was used so that 1 single image contains approximately 75% of a well
501 surface. The exposure time was set at 0.023 seconds, as determined by the fluorescent
502 intensity signal in the control wells. Imaging acquisition speed was optimized using a 2x2
503 binning on 1104x1104 pixel resolution and reducing the number of autofocus focal planes. The
504 Cellomics (ThermoFisher) software was used for image analysis. A custom-made image analysis
505 protocol was created using the SpotDetector bioapplication. First, a background reduction was
506 performed on the raw images to remove non-specific fluorescent signal. Second, a fixed
507 fluorescent intensity threshold was determined to identify eGFP signal. Lastly, the total surface
508 area occupied by eGFP signal was calculated from the processed images. The selected output
509 feature was 'SpotTotalAreaCh2' and was used for further data analysis.

510

511 **Hit selection.** The entire compound collection was screened in two independent experiments.
512 Data were normalized to the median of each plate. The Z-score was calculated on the basis of
513 the $\log_2(\text{fold change})$ ($\log_2\text{FC}$) with the average and standard deviation of each plate. 40
514 compounds from the screen were selected according to the cutoff of fluorescence % area
515 greater than 15 in at least one of the two screens, which is 15 times greater than the values
516 obtained with untreated or DMSO treated cells.

517

518 **Plasmids.** Plasmids used in the production of SARS-CoV-2 pseudovirus were a gift from Jing
519 Lin (Vitalant, San Francisco). Plasmid encoding VEEV TC-83 with a nanoluciferase reporter
520 (VEEV TC-83-Cap-nLuc-Tav) was a gift from Dr. William B. Klimstra (Department of
521 Immunology, University of Pittsburgh)⁵⁴. DENV2 (New Guinea C strain) TSV01 Renilla reporter
522 plasmid (pACYC NGC FL) was a gift from Pei-Yong Shi (University of Texas Medical Branch,
523 Galveston, Texas, USA)⁵⁵. pDONR223-ErbB4 was a gift from William Hahn & David Root
524 (Addgene plasmid # 23875 ; <http://n2t.net/addgene:23875> ; RRID:Addgene_23875)⁵⁶. The ORF
525 was recombined into a gateway compatible pGluc destination vector using Gateway technology
526 (Invitrogen) and the construct was verified using Sanger sequencing. Mutations were introduced
527 by site-directed mutagenesis using the QuikChange Lightning Site-Directed Mutagenesis Kit
528 (Agilent).

529
530 **Viral stocks preparation and/or passaging.** Belgium-GHB-03021 SARS-CoV-2 strain was
531 recovered from a nasopharyngeal swab taken from an asymptomatic patient returning from
532 Wuhan, China early February 2020⁵⁷ and passaged 6 times on Huh7 and Vero E6 cells. Viral
533 titer was quantified by means of endpoint titrations on confluent Vero E6 cell cultures, calculated
534 using the Spearman-Kärber method, and expressed as 50% tissue culture infectious dose
535 (TCID₅₀)/ml. All Belgium-GHB-03021 SARS-CoV-2-related work was conducted in the high-
536 containment BSL3+ facilities of the KU Leuven Rega Institute (3CAPS) under licenses AMV
537 30112018 SBB 219 2018 0892 and AMV 23102017 SBB 219 2017 0589 according to
538 institutional guidelines.

539
540 The USA-WA1/2020 SARS-CoV-2 strain was received from BEI Resources and passaged 3-6
541 times in Vero E6 cells in DMEM supplemented with 2% FBS. Viral stock titers were determined
542 by standard plaque assay on Vero E6 cells, as described⁵⁸.

543
544 VEEV-TC-83-nLuc RNA was transcribed *in vitro* from cDNA plasmid templates linearized with
545 MluI via MEGAscript SP6 kit (Invitrogen #AM1330) and electroporated into BHK-21 cells.
546 Similarly, DENV RNA was transcribed *in vitro* from pACYC-DENV2-NGC plasmid by
547 mMessage/mMachine (Ambion) kits and electroporated into BHK-21 cells. For both viruses, the
548 supernatants were harvested after 24 hours post electroporation, clarified and stored at -80 °C.
549 WT Trinidad Donkey (TrD) VEEV strain, EBOV (Kikwit isolate) and MARV (Ci67 strain) were
550 obtained from BEI Resources. EBOV and MARV were grown in Vero E6 cells. Viral stock titers
551 were determined via standard plaque assays on BHK-21 for DENV and VEEV or on Vero E6
552 cells for EBOV and MARV.

553
554 USA-WA1/2020 SARS-CoV-2- and WT VEEV-related work was conducted in the high-
555 containment BSL3 facilities of Stanford University and George Mason University according to
556 CDC and institutional guidelines. EBOV and MARV work was conducted at the high-
557 containment BSL4 facilities at the United States Army Medical Research Institute of Infectious
558 Diseases.

559
560 **Viral sequencing.** All SARS-CoV-2 stocks were deep sequenced on a MiSeq platform
561 (Illumina).

562 For the HTS of compound library, Belgium/GHB-03021/2020 SARS-CoV-2 from passage 6 (P6)
563 was used. The viral stock was deep sequenced following an established metagenomics pipeline
564 ⁵⁹. 100% of the viral reads of P6 GHB-03021/2020 SARS-CoV-2 harbored a deletion of the
565 multi-basic cleavage (MBC) domain, as reported⁵⁹.

566

567 The rest of the experiments were done using the USA-WA1/2020 strain. SARS-CoV-2 whole-
568 genome amplicon-based sequencing was conducted by adapting an existing whole genome
569 sequencing pipeline for poliovirus genotyping⁶⁰. Dose response curves with lapatinib in Calu-3
570 and Vero cells (**Fig. 1e, 2b and Extended data fig. 2b**) were performed with a P3 USA-
571 WA1/2020 SARS-CoV-2 virus harboring no deletion or point mutations in the MBC domain. The
572 remaining experiments were performed using a P6 USA-WA1/2020 SARS-CoV-2 containing
573 mixed populations, of which the majority (51%-80%) had WT sequence with no MBC deletion.

574 **Cells.** The African green monkey kidney cell line (Vero E6) constitutively expressing the
575 enhanced green fluorescent protein (eGFP) used for antiviral screening purposes was kindly
576 provided by Dr. Marnix Van Loock (Janssen Pharmaceutica, Beerse, Belgium)⁵³. Cells were
577 maintained in Dulbecco's modified Eagle's medium (DMEM; Gibco) supplemented with 10% v/v
578 fetal calf serum (FCS; Biowest), 0.075% sodium bicarbonate (7.5% solution, Gibco) and 1x Pen-
579 strep (Gibco). The assay medium was DMEM, supplemented with 2% FCS. Vero E6 (ATCC)
580 were maintained in DMEM (10-013-CV, Corning) supplemented with 10% fetal bovine serum
581 (FBS, Omega Scientific, Inc), 1% L-glutamine 200mM (Gibco), 1% penicillin-streptomycin
582 (Gibco), 1% nonessential amino acids (Gibco), 1% HEPES (Gibco), 1% Sodium pyruvate
583 (Thermofisher scientific). Vero (ATCC), HEK-293T (ATCC), U-87 MG (ATCC), and BHK-21
584 (ATCC) cells were grown in DMEM (10-013-CV, Corning) supplemented with 10% FBS (Omega
585 Scientific, Inc), and 1% penicillin-streptomycin. Huh7 cells (Apath LLC) and Calu-3 cells (ATCC)
586 were grown in DMEM (10-013-CV, Corning) supplemented with 10% FBS (Omega Scientific,
587 Inc), 1% L-glutamine, 1% nonessential amino acids (Corning) and 1% penicillin-streptomycin
588 (Gibco). All the cells were maintained in a humidified incubator with 5% CO₂ at 37°C. All cells
589 were tested negative for mycoplasma by the MycoAlert mycoplasma detection kit (Lonza,
590 Morristown, NJ).

591 **Human adult lung organoids and organoid-derived monolayers for SARS-CoV-2**

592 **infection.** The human adult lung organoid (ALO) model containing proximal and distal features
593 of airway epithelia was generated from adult stem cells isolated from deep lung biopsy
594 specimens²⁹. The organoids from these lung tissues were isolated and propagated using an
595 approved human research protocol (IRB# 190105: PI Ghosh and Das) that covers human
596 subject research at the UC San Diego HUMANOID Center of Research Excellence (CoRE). The
597 lung organoid model is complete with all 6 cell types of proximal and distal airways as validated
598 previously²⁹. Lung-organoid-derived single cells were prepared²⁹ and plated in Pneumacult Ex-
599 Plus Medium (StemCell, Canada). After 2 days, monolayers were infected with SARS-CoV-2
600 (USA-WA1/2020 strain) at an MOI of 1.

601

602 **rVSV-SARS-CoV-2-S production.** HEK-293T cells were transfected with 30 µg of Spike (S)
603 expression plasmid. Twenty-four hours post-transfection, the medium was replaced and cells

604 were treated with DMEM containing 3.75 mM valproic acid (VPA) for 4 hours. The medium was
605 then removed, and cells were infected with VSV-G pseudotyped Δ G-luciferase VSV virus
606 (MOI=3). Six hours post-infection, cells were washed with PBS and fresh medium containing
607 anti-VSV-G hybridoma was added to neutralize the residual VSV-G pseudovirus. Culture
608 supernatant was harvested after 24-hour incubation, clarified by centrifugation, filtered (0.22
609 μ m) and stored at -80°C . The TCID₅₀ of rVSV-SARS-CoV-2-S pseudovirus was determined via
610 luciferase assay 24 hours after infection of Vero cells. Positive wells were defined as having
611 luminescence unit (RLU) values at least 10-fold higher than the cell background.

612
613 **Western blotting and antibodies.** Cells were lysed in M-Per protein extraction reagent
614 (Thermo Fisher Scientific) or RIPA buffer containing 1% NP40 supplemented with Halt protease
615 and phosphatase inhibitor cocktail (Thermo Fisher Scientific). Clarified lysates were run on 4%–
616 12% Bis-Tris gels (Invitrogen), transferred onto PVDF membranes (Bio-Rad). Blots were
617 blocked with 5% BSA/TBST and blotted with anti-ErbB4 (Santa Cruz), ErbB2 (Cell Signaling),
618 ErbB1, AKT, ERK, p38 (Cell Signaling), P-ErbB4 (Tyr1284), P-ErbB2(Tyr1248), P-AKT(Ser473),
619 P-ERK(Thr202/Tyr204), P-p38 (Thr180/Tyr182) (Cell Signaling), and β -actin (Sigma-Aldrich,
620 catalog A3854) antibodies. Signal was detected with HRP-conjugated secondary antibodies.
621 Band intensity was quantified with ImageJ software (NIH).

622
623 **RNA interference.** siRNAs (10 pmol/96-well) were transfected into cells using lipofectamine
624 RNAiMAX transfection reagent (Invitrogen) 48 hours prior to infection with VEEV-TC-83-nLuc at
625 MOI of 0.01, rVSV-SARS-CoV-2-S or SARS-CoV-2 (USA-WA1/2020). ON-TARGETPlus siRNA
626 SMARTpools against 7 genes and non-targeting siRNA (siNT) were purchased
627 from Dharmacon/Horizon Discovery with gene IDs as follows: EGFR (1956), ErbB2 (2064),
628 ErbB4 (2066), RIPK2 (8767), RAF1 (5894), STK10 (6793), MAP2K5 (5607). Single ErbB4
629 siRNAs were ordered from Millipore Sigma (ErbB#1 GCAAGAAUUGACUCGAAU, ErbB#2
630 CCUCAAGAUACCUAGUUA).

631
632 **Infection assays.** Calu-3 cells, Vero cells or ALOs were infected with SARS-CoV-2 in triplicates
633 (MOI=0.05 or 1) in DMEM containing 2% FCS at 37°C under biosafety level 3 (BSL3)
634 conditions. After 1 to 3-hour incubation, the inoculum was removed, cells were washed and
635 supplemented with new medium. At various time points post-infection, culture supernatants
636 were harvested for measurement of viral titer by standard plaque assays and cells were lysed in
637 Trizol for RT-qPCR analysis. Huh7 cells were infected with DENV2 in replicates ($n = 3$ -10) at an
638 MOI of 0.05. Overall infection was measured at 48 hours using a *Renilla* luciferase substrate or
639 a standard plaque assay. Huh7 cells were infected with EBOV (MOI=1) or MARV (MOI=2)
640 under BSL4 conditions. 48 hours post-infection cells were formalin-fixed for 24 hours prior to
641 removal from BSL4. Infected cells were detected using an EBOV or MARV glycoprotein-specific
642 monoclonal antibody (KZ52 and 7E6, respectively) and quantitated by automated fluorescence
643 microscopy using an Operetta High Content Imaging System and the Harmony software
644 package (PerkinElmer). U-87 MG cells were infected with VEEV-TC-83-nLuc in 8 replicates at
645 MOI of 0.01. Overall infection was measured at 24 hours post-infection via a nanoluciferase
646 assay using a luciferin solution obtained from the hydrolysis of its O-acetylated precursor,
647 hizarazine-103 (prepared by Dr. Yves Janin, Institut Pasteur, France) as a substrate⁶¹ or

648 standard plaque assay. U-87 MG cells were infected with WT VEEV TrD in triplicates and at 24
649 hours post-infection the viral titer was measured via standard plaque assays.

650

651 **Pharmacological inhibition.** Inhibitors or DMSO were added to the cells 1 hour prior to viral
652 inoculation and were left for the duration of the experiment. Viral infection was measured via
653 luciferase (DENV2, VEEV (TC-83)) or plaque (SARS-CoV-2, VEEV-TrD, VEEV (TC-83),
654 DENV2) assays. Immunofluorescence assay with anti-GP probe was used for EBOV and
655 MARV.

656

657 **Entry assays.** Vero cells were infected with virulent SARS-CoV-2 (MOI=1) or a high inoculum
658 of rVSV-SARS-CoV-2-S. Following 1-hour incubation, the viral inoculum was removed, cells
659 were washed three times with PBS and replaced with fresh medium. At 3 hours post-infection,
660 cells were lysed in TRIzol (Invitrogen) or RLT lysis buffer (RNeasy Mini Kit, Qiagen) and viral
661 RNA levels were measured by RT-qPCR.

662

663 **RT-qPCR.** RNA was extracted from cell lysates using Direct-zol RNA Miniprep Plus Kit (Zymo
664 Research) or RNeasy Mini Kit (Qiagen) and reverse transcribed using High-Capacity cDNA RT
665 kit (Applied Biosystems) according to the manufacturer's instructions. Primers and PowerUp
666 SYBR Green Master Mix (Applied Biosystems) were added to the samples, and PCR reactions
667 were performed with QuantStudio3 (Applied Biosystems). Samples were analyzed in triplicates
668 and target genes were normalized to the housekeeping gene. The following primers were used:
669 GAPDH (F-GGAGCGAGATCCCTCCAAAAT; R-GGCTGTTGTCATACTTCTCATGG), ErbB1 (F-
670 ACCACCCTGGTCTGGAAGTACG; R-TCGTTGGACAGCCTTCAAGACC); ErbB2 (F-
671 GGAAGTACACGATGCGGAGACT; R-ACCTTCCTCAGCTCCGTCTCTT); ErbB4 (F-
672 GGAGTATGTCCACGAGCACAAG; R-CGAGTCGTCTTTCTTCCAGGTAC) N-SARS-CoV2 (F-
673 TAATCAGACAAGGAACTGATTA, R-CGAAGGTGTGACTTCCATG).

674

675 **Viability assays.** Viability was assessed using alamarBlue reagent (Invitrogen) according to the
676 manufacturer's protocol. Fluorescence was detected at 560 nm on an InfiniteM1000 plate
677 reader (Tecan).

678

679 **Gain-of-function assays.** Plasmids encoding WT ErbB4, ErbB4 mutant (K751R) or empty
680 control were transfected individually into Vero or U-87 MG cells using Lipofectamine 3000
681 reagent (Invitrogen) 24 hours prior to drug treatment and infection with rVSV-SARS-CoV-2-S or
682 VEEV-TC-83-nLuc, respectively. Viral infection and cell viability were measured 24 hours later
683 via luciferase and alamarBlue assays, respectively.

684

685 **Resistance studies.** VEEV (TC-83) was used to inoculate U-87 MG cells at MOI of 0.1 and
686 passaged every 24 hours by transferring an equal volume of viral supernatant to naive cells
687 under increasing drug selection (2.5-5 μ M, passages 1-3; 5-10 μ M, passages 4-7; 10-15 μ M,
688 passages 8-10). Upon completion of 10 passages, viral titers were measured in culture
689 supernatants by plaque assays. ML336 resistant mutation emerging in nsP2 at passage 10 was
690 confirmed by purification and reverse transcription of viral RNA from cell supernatants using
691 RNeasy Mini Kit (Qiagen) and SuperScript IV First-Strand Synthesis kit (Invitrogen) respectively.

692 The nsP2 region was amplified with Platinum Green Hot Start PCR Master Mix (2x) (Invitrogen)
693 using the following primers: (forward: AGGAAAATGTTAGAGGAGCACAAAG reverse:
694 GTCAATATACAGGGTCTCTACGGGGTGT (and sequenced (Sequetech Corp.).

695
696 **In vitro kinase assays.** ErbB2 and ErbB4 *in vitro* kinase assays were performed on the
697 LabChip platform (Nanosyn) or radiometric HotSpot™ kinase assay platform (Reaction Biology).

698
699 **Signaling pathway analysis.** Following a 2-hour starvation under serum-low or -free
700 conditions, Calu-3 cells or ALOs were treated with lapatinib or DMSO and within an hour
701 infected with SARS-CoV-2 (MOI=1). Cell lysates were obtained at 1.5 and/or 24 hours post-
702 infection followed by Western blot analysis with antibodies targeting the phosphorylated and
703 total forms of ErbB1, 2 and 4, p38/MAPK, ERK, and AKT. Phosphorylated to total protein ratios
704 were quantified with ImageJ software (NIH).

705
706 **Cytokine measurements in culture supernatants.** A LEGENDplex Human Inflammation
707 Panel 1 (Biolegend) kit was used following the manufacturer's instructions to measure the
708 concentration of cytokines in culture supernatants derived from ALOs. Cytokine concentrations
709 were measured via Quanteon (Agilent) and data analyzed using LEGENDplex V8.0 software.

710
711 **Immunofluorescence and confocal microscopy.** ALO cells were plated at a concentration of
712 2.5×10^6 cell/well in a μ -Slide 8 well (ibidi) system. Lapatinib or DMSO were administered either
713 an hour pre-infection or 4 hours post-infection with SARS-CoV-2 (MOI=1). At 24-, 36- and 48-
714 hours post-infection, cells were washed with PBS and fixed with 4% PFA for 30 minutes at RT.
715 Cells were blocked for 1h at RT with 3% BSA and 0.1 % Triton X in PBS. Cells were incubated
716 with mouse mAb SARS-CoV-2 nucleocapsid antibody (SinoBiological, 1:100) and rabbit Claudin
717 7 polyclonal antibody (ThermoFisher, 1:200) overnight at 4°C, followed by 1 hour incubation at
718 room temperature with goat anti-mouse AF488 (ThermoFisher, 1:400), goat anti-rabbit AF647
719 (ThermoFisher, 1:400), and counterstaining with DAPI (4', 6-diamidino-2-phenylindole,
720 ThermoFisher, 1:10000) and phalloidin (ThermoFisher, 1:400). Images were taken on an SP8
721 microscope (Leica). Adjustment for brightness, contrast and color balance were done using Fiji
722 software.

723
724 **Quantification and Statistical Analysis.** All data were analyzed with GraphPad Prism
725 software. Fifty percent effective concentrations (EC₅₀) and 50% cytotoxic concentration (CC₅₀)
726 were measured by fitting of data to a 3-parameter logistic curve. *P* values were calculated by
727 one-way ANOVA with either Dunnett's or Tukey's multiple comparisons tests as specified in
728 each Fig. legend.

729
730
731
732
733
734

735 **References:**

- 736 1 Wu, Z. & McGoogan, J. M. Characteristics of and Important Lessons From the
737 Coronavirus Disease 2019 (COVID-19) Outbreak in China: Summary of a Report of
738 72 314 Cases From the Chinese Center for Disease Control and Prevention. *JAMA* **323**,
739 1239-1242, doi:10.1001/jama.2020.2648 (2020).
- 740 2 Beigel, J. H. *et al.* Remdesivir for the Treatment of Covid-19 - Final Report. *The New*
741 *England journal of medicine*, NEJMoa2007764, doi:10.1056/NEJMoa2007764 (2020).
- 742 3 Horby, P. *et al.* Dexamethasone in Hospitalized Patients with Covid-19 - Preliminary
743 Report. *The New England journal of medicine*, doi:10.1056/NEJMoa2021436 (2020).
- 744 4 Spagnolo, P. *et al.* Pulmonary fibrosis secondary to COVID-19: a call to arms? *The*
745 *Lancet. Respiratory medicine* **8**, 750-752, doi:10.1016/S2213-2600(20)30222-8 (2020).
- 746 5 Jin, Z. *et al.* Structure of Mpro from COVID-19 virus and discovery of its inhibitors.
747 *Nature*, doi:10.1038/s41586-020-2223-y (2020).
- 748 6 Riva, L. *et al.* Discovery of SARS-CoV-2 antiviral drugs through large-scale compound
749 repurposing. *Nature* **586**, 113-119, doi:10.1038/s41586-020-2577-1 (2020).
- 750 7 Gordon, D. E. *et al.* A SARS-CoV-2 protein interaction map reveals targets for drug
751 repurposing. *Nature* **583**, 459-468, doi:10.1038/s41586-020-2286-9 (2020).
- 752 8 Bouhaddou, M. *et al.* The Global Phosphorylation Landscape of SARS-CoV-2 Infection.
753 *Cell* **182**, 685-712.e619, doi:10.1016/j.cell.2020.06.034 (2020).
- 754 9 Saul, S. & Einav, S. Old Drugs for a New Virus: Repurposed Approaches for Combating
755 COVID-19. *ACS infectious diseases*, doi:10.1021/acsinfecdis.0c00343 (2020).
- 756 10 Ivens, T. *et al.* Development of a homogeneous screening assay for automated
757 detection of antiviral agents active against severe acute respiratory syndrome-
758 associated coronavirus. *J Virol Methods* **129**, 56-63, doi:10.1016/j.jviromet.2005.05.010
759 (2005).
- 760 11 Ianevski, A. *et al.* Potential Antiviral Options against SARS-CoV-2 Infection. *Viruses* **12**,
761 doi:10.3390/v12060642 (2020).
- 762 12 Chen, J., Kinoshita, T., Sukbuntherng, J., Chang, B. Y. & Elias, L. Ibrutinib Inhibits ERBB
763 Receptor Tyrosine Kinases and HER2-Amplified Breast Cancer Cell Growth. *Mol Cancer*
764 *Ther* **15**, 2835-2844, doi:10.1158/1535-7163.Mct-15-0923 (2016).
- 765 13 Levitzki, A. & Gazit, A. Tyrosine kinase inhibition: an approach to drug development.
766 *Science* **267**, 1782-1788, doi:10.1126/science.7892601 (1995).
- 767 14 Chung, D. *et al.* in *Probe Reports from the NIH Molecular Libraries Program* (National
768 Center for Biotechnology Information (US), 2010).

- 769 15 Finigan, J. H., Downey, G. P. & Kern, J. A. Human epidermal growth factor receptor
770 signaling in acute lung injury. *American journal of respiratory cell and molecular biology*
771 **47**, 395-404, doi:10.1165/rcmb.2012-0100tr (2012).
- 772 16 Qiu, C. *et al.* Mechanism of activation and inhibition of the HER4/ErbB4 kinase.
773 *Structure (London, England : 1993)* **16**, 460-467, doi:10.1016/j.str.2007.12.016 (2008).
- 774 17 Rusnak, D. W. *et al.* The effects of the novel, reversible epidermal growth factor
775 receptor/ErbB-2 tyrosine kinase inhibitor, GW2016, on the growth of human normal and
776 tumor-derived cell lines in vitro and in vivo. *Mol Cancer Ther* **1**, 85-94 (2001).
- 777 18 Hickinson, D. M. *et al.* AZD8931, an Equipotent, Reversible Inhibitor of Signaling by
778 Epidermal Growth Factor Receptor, ERBB2 (HER2), and ERBB3: A Unique Agent for
779 Simultaneous ERBB Receptor Blockade in Cancer. *Clinical Cancer Research* **16**, 1159-
780 1169, doi:10.1158/1078-0432.Ccr-09-2353 (2010).
- 781 19 Finigan, J. H. *et al.* Neuregulin-1-human epidermal receptor-2 signaling is a central
782 regulator of pulmonary epithelial permeability and acute lung injury. *The Journal of*
783 *biological chemistry* **286**, 10660-10670, doi:10.1074/jbc.M110.208041 (2011).
- 784 20 Ma, X., Yu, X. & Zhou, Q. The IL1 β -HER2-CLDN18/CLDN4 axis mediates lung barrier
785 damage in ARDS. *Aging (Albany NY)* **12**, 3249-3265, doi:10.18632/aging.102804
786 (2020).
- 787 21 Faress, J. A. *et al.* Bleomycin-induced pulmonary fibrosis is attenuated by a monoclonal
788 antibody targeting HER2. *Journal of applied physiology (Bethesda, Md. : 1985)* **103**,
789 2077-2083, doi:10.1152/jappphysiol.00239.2007 (2007).
- 790 22 Finigan, J. H. *et al.* HER2 activation results in β -catenin-dependent changes in
791 pulmonary epithelial permeability. *American journal of physiology. Lung cellular and*
792 *molecular physiology* **308**, L199-207, doi:10.1152/ajplung.00237.2014 (2015).
- 793 23 Hardie, W. D. *et al.* Reversal of lung lesions in transgenic transforming growth factor
794 alpha mice by expression of mutant epidermal growth factor receptor. *American journal*
795 *of respiratory cell and molecular biology* **15**, 499-508, doi:10.1165/ajrcmb.15.4.8879184
796 (1996).
- 797 24 Zhou, Y. *et al.* Amphiregulin, an epidermal growth factor receptor ligand, plays an
798 essential role in the pathogenesis of transforming growth factor- β -induced pulmonary
799 fibrosis. *The Journal of biological chemistry* **287**, 41991-42000,
800 doi:10.1074/jbc.M112.356824 (2012).
- 801 25 Li, R. *et al.* HMGB1/PI3K/Akt/mTOR Signaling Participates in the Pathological Process
802 of Acute Lung Injury by Regulating the Maturation and Function of Dendritic Cells.
803 *Frontiers in Immunology* **11**, doi:10.3389/fimmu.2020.01104 (2020).
- 804 26 Zhang, X. L., Xing, R. G., Chen, L., Liu, C. R. & Miao, Z. G. PI3K/Akt signaling is
805 involved in the pathogenesis of bleomycin-induced pulmonary fibrosis via regulation of
806 epithelial-mesenchymal transition. *Molecular medicine reports* **14**, 5699-5706,
807 doi:10.3892/mmr.2016.5960 (2016).

- 808 27 Zarubin, T. & Han, J. Activation and signaling of the p38 MAP kinase pathway. *Cell*
809 *research* **15**, 11-18, doi:10.1038/sj.cr.7290257 (2005).
- 810 28 Appelberg, S. *et al.* Dysregulation in Akt/mTOR/HIF-1 signaling identified by proteo-
811 transcriptomics of SARS-CoV-2 infected cells. *Emerging Microbes & Infections* **9**, 1748-
812 1760, doi:10.1080/22221751.2020.1799723 (2020).
- 813 29 Tindle, C. *et al.* Adult Stem Cell-derived Complete Lung Organoid Models Emulate Lung
814 Disease in COVID-19. *bioRxiv*, doi:10.1101/2020.10.17.344002 (2020).
- 815 30 Del Valle, D. M. *et al.* An inflammatory cytokine signature predicts COVID-19 severity
816 and survival. *Nature medicine* **26**, 1636-1643, doi:10.1038/s41591-020-1051-9 (2020).
- 817 31 Sokol, C. L. & Luster, A. D. The chemokine system in innate immunity. *Cold Spring*
818 *Harbor perspectives in biology* **7**, doi:10.1101/cshperspect.a016303 (2015).
- 819 32 Bekerman, E. & Einav, S. Combating emerging viral threats. *Science* **348**, 282-283,
820 doi:10.1126/science.aaa3778 (2015).
- 821 33 Raymonda, M. H. *et al.* Pharmacologic profiling reveals lapatinib as a novel antiviral
822 against SARS-CoV-2 in vitro. *bioRxiv*, 2020.2011.2025.398859,
823 doi:10.1101/2020.11.25.398859 (2020).
- 824 34 O'Donovan, S. M. *et al.* Identification of candidate repurposable drugs to combat
825 COVID-19 using a signature-based approach. *Scientific Reports* **11**, 4495,
826 doi:10.1038/s41598-021-84044-9 (2021).
- 827 35 Selvaraj, G., Kaliyamurthi, S., Peslherbe, G. & Wei, D. Identifying potential drug targets
828 and candidate drugs for COVID-19: biological networks and structural modeling
829 approaches [version 1; peer review: 1 approved with reservations]. *F1000Research* **10**,
830 doi:10.12688/f1000research.50850.1 (2021).
- 831 36 Mizutani, T., Fukushi, S., Saijo, M., Kurane, I. & Morikawa, S. Phosphorylation of p38
832 MAPK and its downstream targets in SARS coronavirus-infected cells. *Biochem Biophys*
833 *Res Commun* **319**, 1228-1234, doi:10.1016/j.bbrc.2004.05.107 (2004).
- 834 37 Kindrachuk, J. *et al.* Antiviral Potential of ERK/MAPK and PI3K/AKT/mTOR Signaling
835 Modulation for Middle East Respiratory Syndrome Coronavirus Infection as Identified by
836 Temporal Kinome Analysis. *Antimicrobial agents and chemotherapy* **59**, 1088-1099,
837 doi:10.1128/AAC.03659-14 (2015).
- 838 38 Venkataraman, T., Coleman, C. M. & Frieman, M. B. Overactive Epidermal Growth
839 Factor Receptor Signaling Leads to Increased Fibrosis after Severe Acute Respiratory
840 Syndrome Coronavirus Infection. *Journal of virology* **91**, e00182-00117,
841 doi:10.1128/jvi.00182-17 (2017).
- 842 39 Bierman, A., Yerrapureddy, A., Reddy, N. M., Hassoun, P. M. & Reddy, S. P. Epidermal
843 growth factor receptor (EGFR) regulates mechanical ventilation-induced lung injury in
844 mice. *Transl Res* **152**, 265-272, doi:10.1016/j.trsl.2008.10.004 (2008).

- 845 40 Ishii, Y., Fujimoto, S. & Fukuda, T. Gefitinib prevents bleomycin-induced lung fibrosis in
846 mice. *American journal of respiratory and critical care medicine* **174**, 550-556,
847 doi:10.1164/rccm.200509-1534OC (2006).
- 848 41 Hardie, W. D. *et al.* EGF receptor tyrosine kinase inhibitors diminish transforming growth
849 factor- α -induced pulmonary fibrosis. *American Journal of Physiology-Lung Cellular and*
850 *Molecular Physiology* **294**, L1217-L1225, doi:10.1152/ajplung.00020.2008 (2008).
- 851 42 Freeman, M. C., Peek, C. T., Becker, M. M., Smith, E. C. & Denison, M. R.
852 Coronaviruses Induce Entry-Independent, Continuous Macropinocytosis. *mBio* **5**,
853 e01340-01314, doi:10.1128/mBio.01340-14 (2014).
- 854 43 Li, S.-W. *et al.* SARS coronavirus papain-like protease induces Egr-1-dependent up-
855 regulation of TGF- β 1 via ROS/p38 MAPK/STAT3 pathway. *Scientific Reports* **6**, 25754,
856 doi:10.1038/srep25754 (2016).
- 857 44 Koka, V. *et al.* Angiotensin II up-regulates angiotensin I-converting enzyme (ACE), but
858 down-regulates ACE2 via the AT1-ERK/p38 MAP kinase pathway. *The American journal*
859 *of pathology* **172**, 1174-1183, doi:10.2353/ajpath.2008.070762 (2008).
- 860 45 Simões e Silva, A. C., Silveira, K. D., Ferreira, A. J. & Teixeira, M. M. ACE2,
861 angiotensin-(1-7) and Mas receptor axis in inflammation and fibrosis. *Br J Pharmacol*
862 **169**, 477-492, doi:10.1111/bph.12159 (2013).
- 863 46 Akhtar, S. *et al.* Transactivation of ErbB Family of Receptor Tyrosine Kinases Is Inhibited
864 by Angiotensin-(1-7) via Its Mas Receptor. *PloS one* **10**, e0141657-e0141657,
865 doi:10.1371/journal.pone.0141657 (2015).
- 866 47 Kuba, K. *et al.* A crucial role of angiotensin converting enzyme 2 (ACE2) in SARS
867 coronavirus-induced lung injury. *Nature medicine* **11**, 875-879, doi:10.1038/nm1267
868 (2005).
- 869 48 Treon, S. P. *et al.* The BTK inhibitor ibrutinib may protect against pulmonary injury in
870 COVID-19-infected patients. *Blood* **135**, 1912-1915, doi:10.1182/blood.2020006288
871 (2020).
- 872 49 Hudachek, S. F. & Gustafson, D. L. Physiologically based pharmacokinetic model of
873 lapatinib developed in mice and scaled to humans. *Journal of pharmacokinetics and*
874 *pharmacodynamics* **40**, 157-176, doi:10.1007/s10928-012-9295-8 (2013).
- 875 50 Neveu, G. *et al.* Identification and Targeting of an Interaction between a Tyrosine Motif
876 within Hepatitis C Virus Core Protein and AP2M1 Essential for Viral Assembly. *PLoS*
877 *pathogens* **8**, e1002845 (2012).
- 878 51 Bekerman, E. *et al.* Anticancer kinase inhibitors impair intracellular viral trafficking and
879 exert broad-spectrum antiviral effects. *The Journal of clinical investigation* **127**,
880 doi:10.1172/JCI89857 (2017).
- 881 52 Wang, P.-G., Tang, D.-J., Hua, Z., Wang, Z. & An, J. Sunitinib reduces the infection of
882 SARS-CoV, MERS-CoV and SARS-CoV-2 partially by inhibiting AP2M1
883 phosphorylation. *Cell Discovery* **6**, 71, doi:10.1038/s41421-020-00217-2 (2020).

- 884 53 Ivens, T. *et al.* Development of a homogeneous screening assay for automated
885 detection of antiviral agents active against severe acute respiratory syndrome-
886 associated coronavirus. *Journal of virological methods* **129**, 56-63,
887 doi:<https://doi.org/10.1016/j.jviromet.2005.05.010> (2005).
- 888 54 Sun, C., Gardner, C. L., Watson, A. M., Ryman, K. D. & Klimstra, W. B. Stable, high-
889 level expression of reporter proteins from improved alphavirus expression vectors to
890 track replication and dissemination during encephalitic and arthritogenic disease. *Journal*
891 *of virology* **88**, 2035-2046, doi:10.1128/JVI.02990-13 (2014).
- 892 55 Zou, G., Xu, H. Y., Qing, M., Wang, Q.-Y. & Shi, P.-Y. Development and characterization
893 of a stable luciferase dengue virus for high-throughput screening. *Antiviral research* **91**,
894 11-19, doi:<http://dx.doi.org/10.1016/j.antiviral.2011.05.001> (2011).
- 895 56 Johannessen, C. M. *et al.* COT drives resistance to RAF inhibition through MAP kinase
896 pathway reactivation. *Nature* **468**, 968-972, doi:10.1038/nature09627 (2010).
- 897 57 Spiteri, G. *et al.* First cases of coronavirus disease 2019 (COVID-19) in the WHO
898 European Region, 24 January to 21 February 2020. *Euro Surveill* **25**, doi:10.2807/1560-
899 7917.Es.2020.25.9.2000178 (2020).
- 900 58 Case, J. B., Bailey, A. L., Kim, A. S., Chen, R. E. & Diamond, M. S. Growth, detection,
901 quantification, and inactivation of SARS-CoV-2. *Virology* **548**, 39-48,
902 doi:<https://doi.org/10.1016/j.virol.2020.05.015> (2020).
- 903 59 Boudewijns, R. *et al.* STAT2 signaling as double-edged sword restricting viral
904 dissemination but driving severe pneumonia in SARS-CoV-2 infected hamsters. *bioRxiv*,
905 2020.2004.2023.056838, doi:10.1101/2020.04.23.056838 (2020).
- 906 60 Sahoo, M. K. *et al.* Detection of Emerging Vaccine-Related Polioviruses by Deep
907 Sequencing. *Journal of clinical microbiology* **55**, 2162-2171, doi:10.1128/jcm.00144-17
908 (2017).
- 909 61 Coutant, E. P. *et al.* Gram-scale synthesis of luciferins derived from coelenterazine and
910 original insights into their bioluminescence properties. *Organic & biomolecular chemistry*
911 **17**, 3709-3713, doi:10.1039/c9ob00459a (2019).
- 912
- 913
- 914
- 915
- 916
- 917
- 918
- 919
- 920

921 **Acknowledgements**

922 This work was supported by a gift from Frank Quattrone and Denise Foderaro (to SE), award
923 number HDTRA11810039 from the Defense Threat Reduction Agency (DTRA)/Fundamental
924 Research to Counter Weapons of Mass Destruction (to SE, SDJ and AN), award number
925 W81XWH-16-1-0691 from the Department of Defense (DoD)/Congressionally Directed Medical
926 Research Programs (CDMRP) (to SE and SDJ), and by the National Institutes for Health (NIH)
927 grants 3R01DK107585-05S1 (to SD), UCOP-R00RG2642 (to SD and PG), and UCOP-
928 R01RG3780 (to PG and DS). Flow cytometry analysis and IF confocal microscopy for this
929 project were done on instruments in the Stanford Shared FACS Facility and Stanford Cell
930 Science Imaging Facility (CSIF) respectively. We thank the Stanford SPARK program's advisors
931 for critical advice and investigators who have provided plasmids (see Methods). We also thank
932 the staff of Stanford Clinical Virology Laboratory for their help sequencing the SARS-CoV-2
933 USA-WA1/2020 isolate used in this work. Opinions, conclusions, interpretations, and
934 recommendations are those of the authors and are not necessarily endorsed by the U.S. Army.
935 The mention of trade names or commercial products does not constitute endorsement or
936 recommendation for use by the Department of the Army or the Department of Defense.

937

938

939 **Author Contributions**

940 S.S., M.K, P.T.H, L.G., W.C., S.K, P.L., N.B, C.C., K.H, M.L. designed and performed the
941 experiments and conducted data analysis. C.T., S.D., P.G., D.S.C, J.J., provided reagents and
942 guidance. S.E., S.D.J., J.D., D.J., J.N, A.N, and B.A.P. provided scientific oversight and
943 guidance. S.E, S.S., S.D.J, M.K. W.C, and D.J. wrote the first version of the manuscript. S.E.,
944 D.J., J.N., A.N., S.D.J. provided funding for the studies.

945

946

947 **Competing interests**

948 The authors declare no competing interests.

949

950

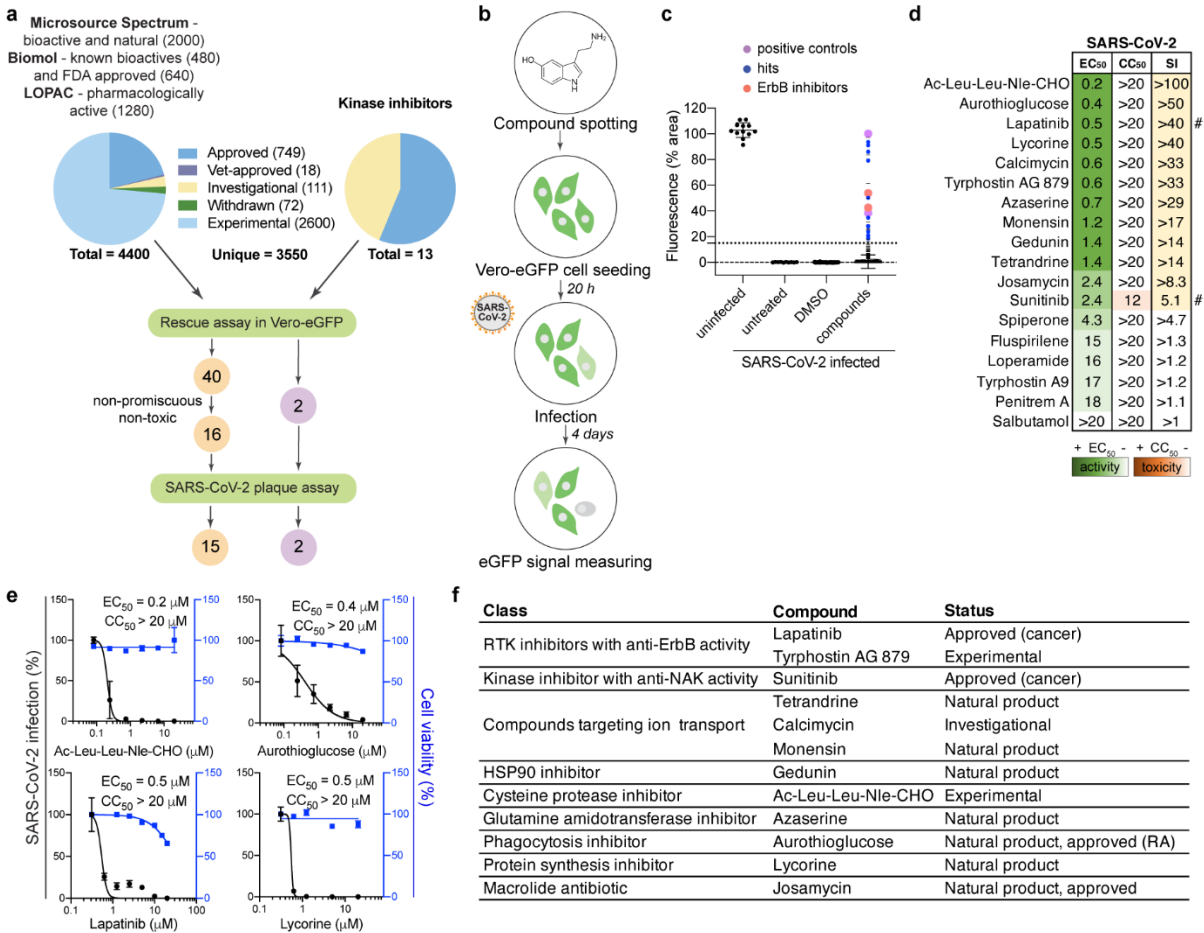
951

952

953

954

955 **Figures**



956
 957
 958
 959
 960
 961
 962
 963
 964
 965
 966
 967
 968
 969
 970
 971
 972
 973
 974
 975
 976
 977

Figure 1. High-throughput screening (HTS) for compounds that counteract SARS-CoV-2-induced lethality and validation by plaque assays.

a, A Schematic of the screening and hit selection pipeline and the composition of the screened libraries. **b**, HTS assay schematic. Compounds were pre-spotted in 384-well plates at a final concentration of 10 μ M. Next, Vero E6 cells constitutively expressing eGFP were added to each well and pre-incubated for 20 hours with the compounds, followed by SARS-CoV-2 infection (Belgium-GHB-03021, MOI = 0.001). eGFP signal measured at 4 days post-infection was used as an indicator for survival from viral-induced lethality. **c**, Boxplots of the percentage of fluorescence area values combining the entire HTS data set (two independent experiments) split into the four indicated categories. The box horizontal lines indicate the first, second (median), and third quartiles. Outliers above a cutoff of 15% were defined as positive hits. Dots represent individual compounds and colors denote positive controls (purple), new hits (blue), and ErbB inhibitors (peach). **d**, Heat map of the EC₅₀ and CC₅₀ values of hits emerging in the HTS color-coded based on the antiviral activity measured by plaque assays (green) and toxicity measured by alamarBlue assays (orange) 24 hours post-infection of Vero cells with SARS-CoV-2 (USA-WA1/2020 strain; MOI=0.05). Selectivity indices (SI) greater than 5 are depicted in yellow. # indicates compounds from the 13-kinase set that also protect from SARS-CoV-2 lethality in the HTS. **e**, Representative dose-response curves of hits depicting SARS-CoV-2 infection (black) and cell viability (blue). Data are relative to DMSO. **f**, The 12 most promising compounds emerging in the HTS.

978 Data in **panels d, e** are representative of 2 or more independent experiments. Individual
979 experiments had 3 biological replicates. Shown are means \pm SD. RA, Rheumatoid arthritis;
980 RTK, receptor tyrosine kinase; NAK, NUMB-associated kinase.
981
982
983

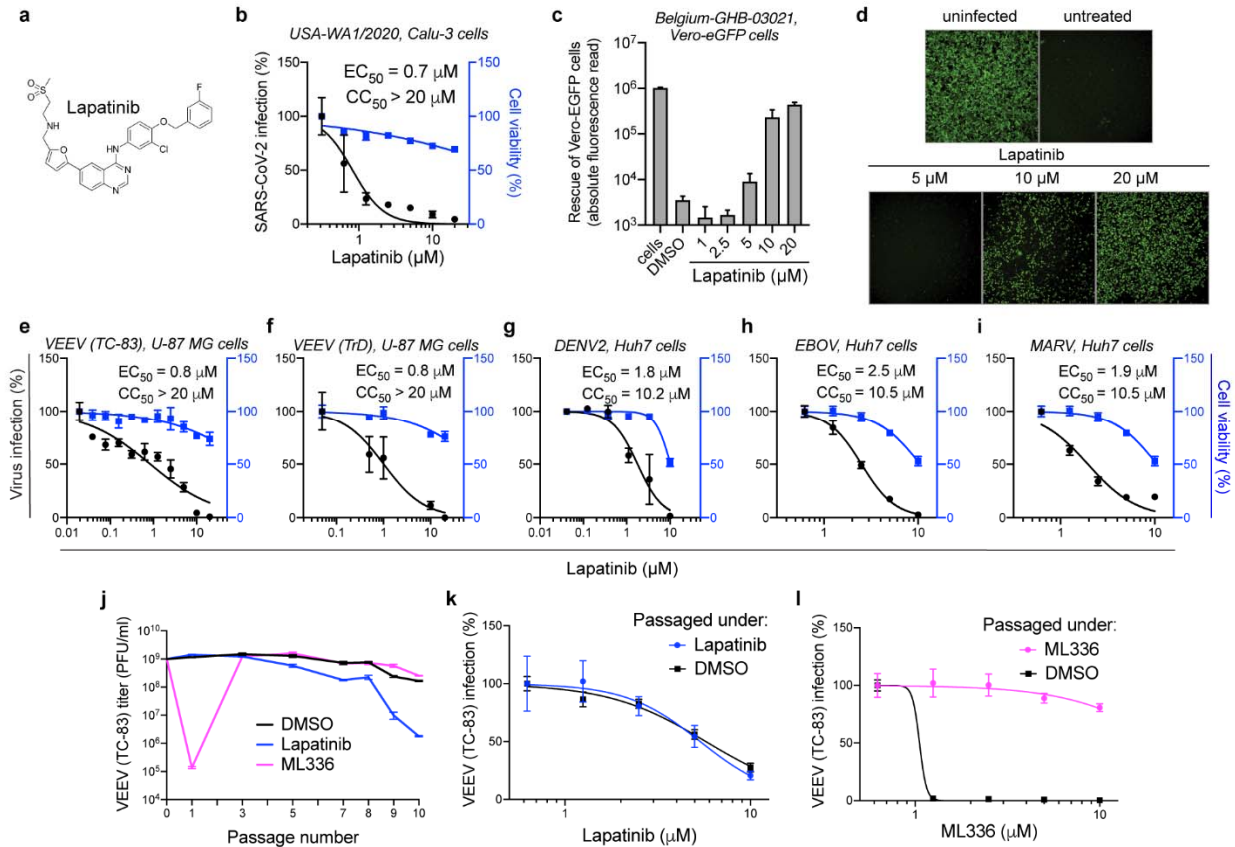
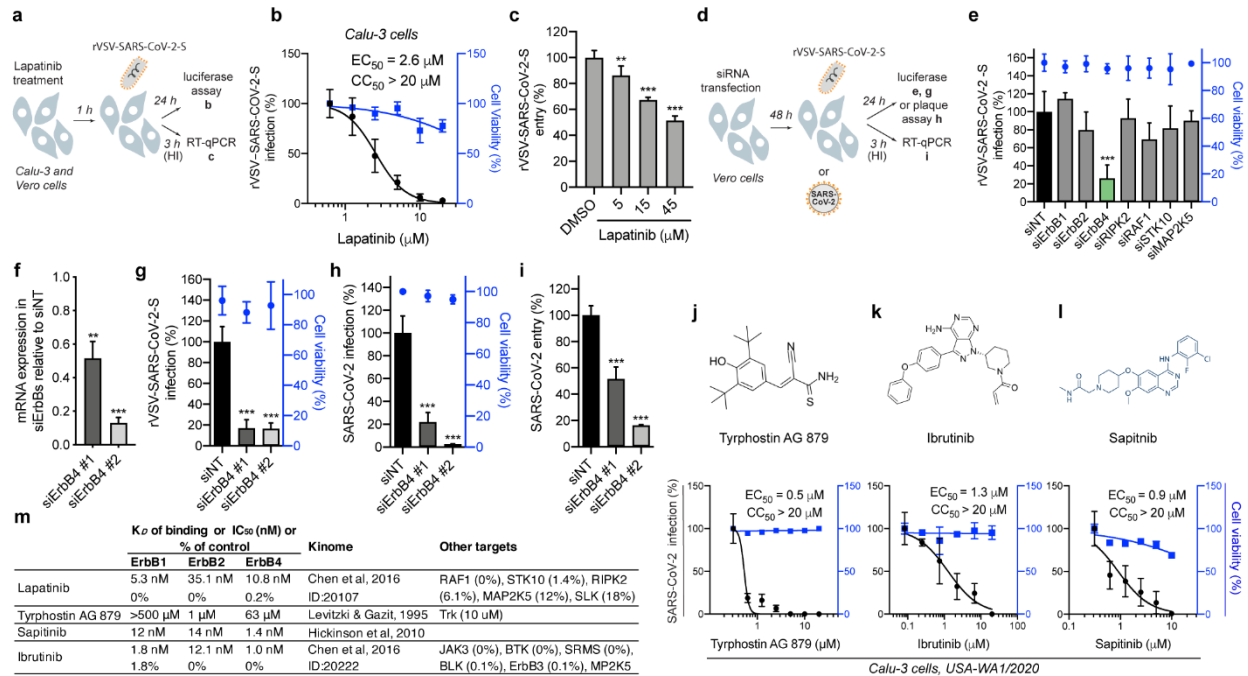


Figure 2. Lapatinib is a potent broad-spectrum antiviral with a high genetic barrier to resistance.

a, Chemical structure of lapatinib. **b**, Dose response to lapatinib of SARS-CoV-2 infection (black, USA-WA1/2020 strain; MOI=0.05) and cell viability (blue) in Calu-3 cells measured via plaque and alamarBlue assays at 24 hours post-infection, respectively. **c**, **d**, Dose-dependent graph (**c**) and corresponding fluorescence images (**d**) of Vero-eGFP cells rescued from SARS-CoV-2-induced lethality by lapatinib at 96 hours post-infection (Belgium-GHB-03021 strain; MOI=0.05). **e**, **f**, Dose response to lapatinib of infection with vaccine (TC-83) (**e**) and WT (Trinidad donkey (TrD)) (**f**) VEEV strains (MOI=0.1) in U-87 MG cells via plaque and alamarBlue assays at 24 hours post-infection, respectively. **g**, Dose response of DENV2 infection (blue) and cellular viability (black) to lapatinib measured in Huh7 cells via plaque and alamarBlue assays at 24 hours post-infection (MOI=0.1), respectively. **h**, **i** Dose response of EBOV (Kikwit isolate, MOI=1) (**h**) and MARV (Ci67 strain, MOI=2) (**i**) infections (blue) and cellular viability (black) to lapatinib measured in Huh7 cells 48 hours post-infection via microneutralization assay and CellTiter-Glo luminescent cell viability assay, respectively. **j**, VEEV (TC-83) was used to infect U-87 MG cells (MOI=0.1) and was then passaged every 24 hours by inoculation of naive U-87 MG cells with equal volumes of viral supernatants under DMSO treatment or selection with lapatinib or ML336 (VEEV nSP2 inhibitor) increasing from 2.5 to 15 μM over 10 passages. Viral titers were measured by plaque assays. **k**, **l**, Dose response to lapatinib (**k**) and ML336 (**l**) of VEEV (TC-83) harvested after 10 passages in U-87 MG cells in the presence of lapatinib (**k**) and ML336 (**l**), via luciferase assays. Data are representative of at least 2 experiments. All panels except J had 2 and 3 biological replicates. Means \pm SD are shown. Data in **b**, **e-i**, **k** and **l** are relative to DMSO.



1010

1011 **Figure 3. ErbB4, but not other lapatinib's targets, is essential for SARS-CoV-2 entry.**
 1012 **a**, Schematic of the experiments shown in panels **b** and **c**. **b**, Dose response to lapatinib of
 1013 rVSV-SARS-CoV-2-S infection (black) and cell viability (blue) in Calu-3 cells via luciferase and
 1014 alamarBlue assays at 24 hours post-infection with a standard inoculum, respectively. **c**, Dose
 1015 response to lapatinib of rVSV-SARS-CoV-2-S entry in Vero cells measured by RT-qPCR at 3
 1016 hours post-infection with a high inoculum (HI). **d**, Schematic of the experiments shown in panels
 1017 **e**, **g**, **h**, **i**. **e**, rVSV-SARS-CoV-2-S infection by luciferase assays (black) and cell viability by
 1018 alamarBlue assays (blue) measured at 24 hours post-infection of Vero cells transfected with the
 1019 indicated siRNA pools. **f**, Confirmation of gene expression knockdown by RT-qPCR in Vero
 1020 cells at 48 hours post-transfection. **g**, rVSV-SARS-CoV-2-S infection (MOI=0.1) measured by
 1021 luciferase assays at 24 hours post-infection of Vero cells transfected with the indicated siRNAs,
 1022 respectively. Shown in blue is cell viability by alamarBlue assays. **h**, SARS-CoV-2 infection at
 1023 24 hours post-infection of ErbB4-depleted Vero cells with SARS-CoV-2 (USA-WA1/2020 strain;
 1024 MOI=0.05) measured by plaque assays. **i**, SARS-CoV-2 entry at 3 hours post-infection of Vero
 1025 cells (MOI=1) measured by RT-qPCR. **j-l**, Chemical structures and dose response to tyrphostin
 1026 AG 879 (**j**), ibrutinib (**k**) and sapitinib (**l**) of SARS-CoV-2 infection (black, USA-WA1/2020 strain;
 1027 MOI=0.05) by plaque assays and cell viability (blue) by alamarBlue assays at 24 hours post-
 1028 infection of Calu-3 cells. **m**, Binding affinity (K_D), enzymatic activity (IC_{50}) or percent binding of
 1029 control (% control) of the indicated kinase inhibitors on the 3 catalytic ErbBs, the source of
 1030 kinome data, and other targets these compounds bind and/or inhibit.
 1031 Data in all panels are representative of 2 or more independent experiments. Individual
 1032 experiments had 3 biological replicates, means \pm SD are shown. ** $P < 0.01$, *** $P < 0.001$
 1033 relative to DMSO (**b**, **c**, **j-l**) or to siNT (**e-i**) (one-way ANOVA followed by Dunnett's multiple
 1034 comparisons test).
 1035

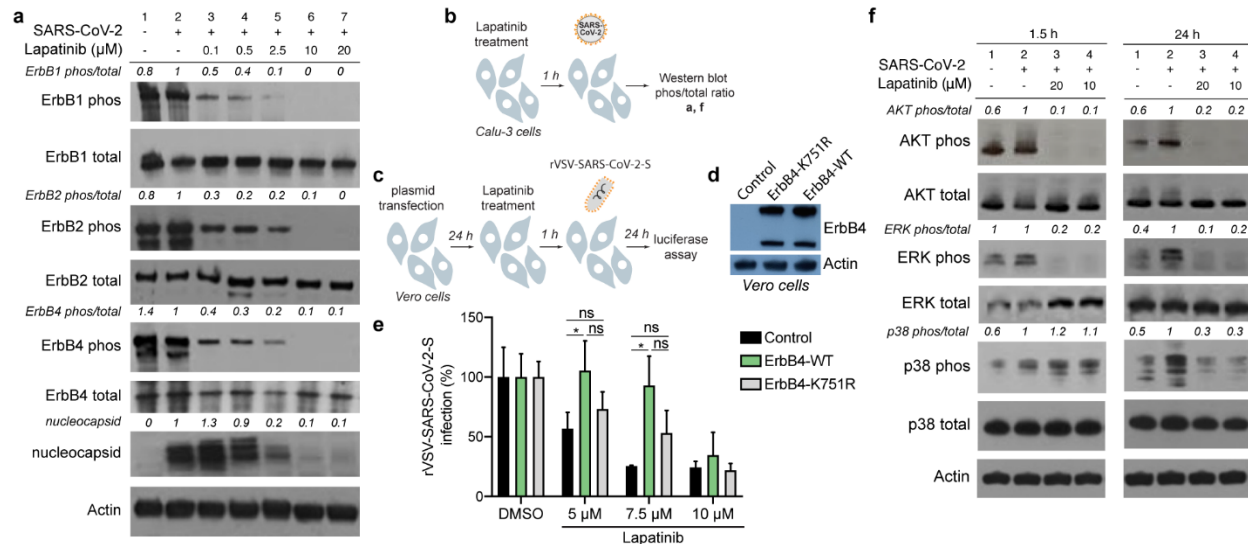


Figure 4. Lapatinib's antiviral activity is associated with functional inhibition of ErbB activity and downstream inflammatory and tissue injury signals and is mediated by ErbB4.

a, ErbB1, 2 and 4 phosphorylation in Calu-3 cells that are uninfected (lane 1), infected and treated with DMSO (lane 2) or infected and treated with increasing concentrations of lapatinib (lanes 3-7) measured by Western blotting 24 hours post-infection with SARS-CoV-2 (USA-WA1/2020 strain, MOI=1). **b**, Schematic of experiments shown in **a**, **f**. **c**, Schematic of the experiments shown in **d**, **e**. **d**, Level of ErbB4 and actin expression measured by Western blot following transfection of Vero cells with control or ErbB4-expressing plasmids. **e**, Rescue of rVSV-SARS-CoV-2-S infection in the presence of lapatinib upon ectopic expression of the indicated plasmids measured by luciferase assays 24 hours after infection in Vero cells. **f**, AKT, ERK, and p38 MAPK phosphorylation in Calu-3 cells that are uninfected (lane 1), infected and treated with DMSO (lane 2) or infected and treated with lapatinib (lanes 3 and 4) measured by Western blotting 1.5 hours and 24 hours post-infection with SARS-CoV-2 (USA-WA1/2020 strain, MOI=1). Shown are representative membranes blotted for phospho- and total proteins and quantitative phospho- to total protein ratio data relative to infected cells treated with DMSO (lane 2) (**a**, **f**). In panel **e** means±SD of results of two combined experiments conducted each with three replicates are shown. **P* < 0.05 relative to DMSO by one-way ANOVA followed by Tukey's multiple comparisons test at each lapatinib concentration (**e**). Ns, non-significant.

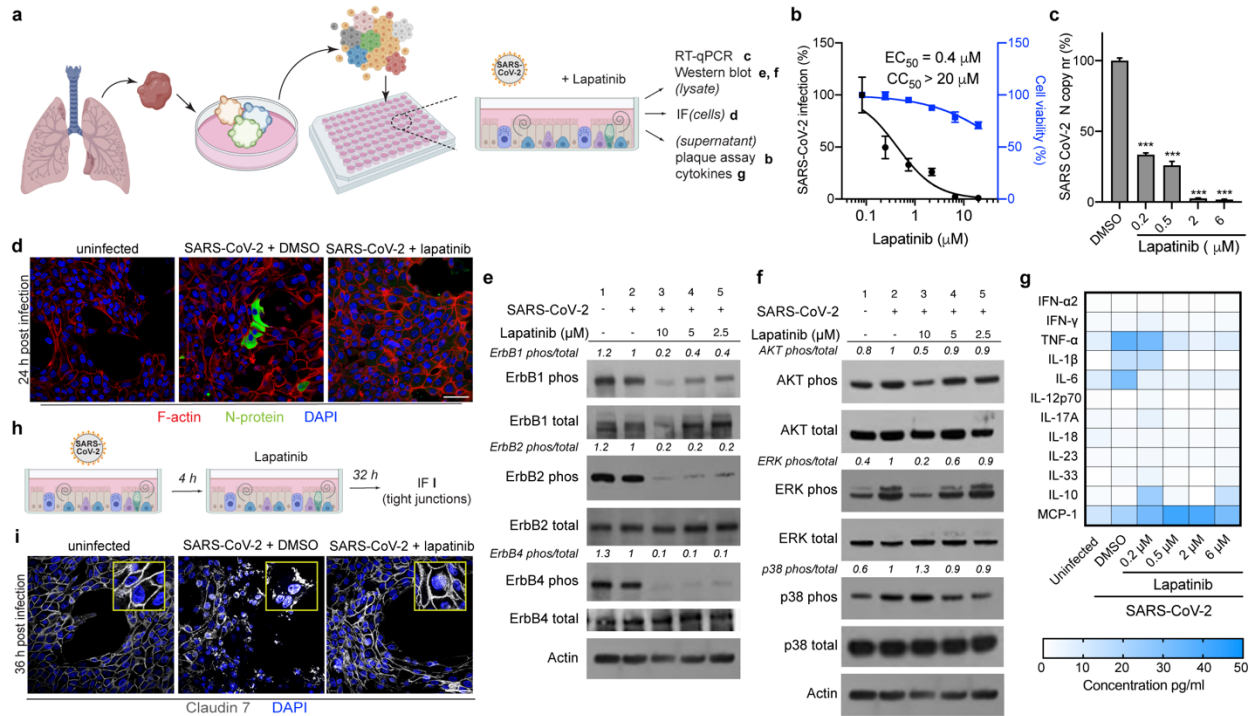
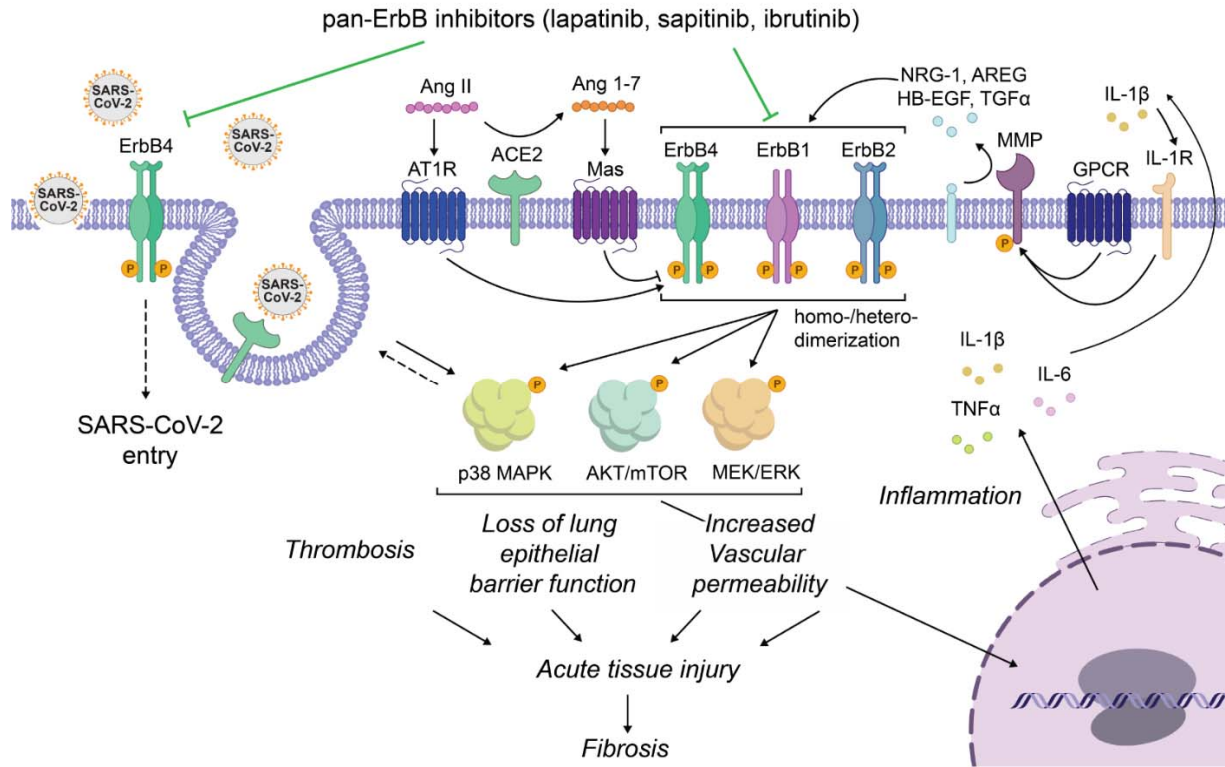


Fig. 5. Lapatinib inhibits SARS-CoV-2 infection, inflammation, and tissue injury ex vivo in human adult lung organoids (ALOs).

a, Schematic of the ALO model and the experimental procedures. ALOs were infected with virulent SARS-CoV-2 (USA-WA1/2020 strain, MOI=1). **b**, Dose response to lapatinib of SARS-CoV-2 infection (black) and cell viability (blue) in ALO supernatants measured via plaque and alamarBlue assays at 48 hours post-infection, respectively. **c**, Dose response to lapatinib of SARS-CoV-2 nucleocapsid (N) copy number in ALO lysates measured by RT-qPCR assays at 48 hours post-infection. **d**, Confocal IF microscopy images of F-actin (red), SARS-CoV-2 nucleocapsid (green) and DAPI (blue) in naive and SARS-CoV-2-infected ALOs pre-treated with DMSO or 10 μM lapatinib 24 hours post-infection. **e, f**, Dose-dependent effect of lapatinib treatment on ErbB1, 2 and 4 (**e**) and AKT, ERK and p38 MAPK (**f**) phosphorylation in ALOs that are uninfected (lane 1), SARS-CoV-2-infected and treated with DMSO (lane 2) or infected and treated with lapatinib (lanes 3-5) measured by Western blotting 48 hours post-infection. Shown are representative membranes blotted for phospho- and total kinases and actin and quantitative phospho- to total kinase ratio data relative to infected ALOs treated with DMSO (lane 2). **g**, Heat map showing the concentration of cytokines (pg/mL) in the supernatants of ALOs under the indicated conditions at 48 hours post-infection with SARS-CoV-2 measured by LEGENDplex (Biolegend) kit. **h**, Schematic of the experiment shown in i. **i**, Confocal IF microscopy images of Claudin 7 (grey) and DAPI (blue) in naive or SARS-CoV-2-infected ALOs treated at 4 hours post-infection either with DMSO or 10 μM lapatinib and imaged at 36 hours post-infection. Data in all panels are representative of 2 or more independent experiments. Individual experiments had 3 biological replicates, means ± SD are shown in panels **b** and **c**. Representative merged images at 40x magnification are shown in panels **d** and **i**. Scale bars are 50 μm. *P < 0.05, **P < 0.01, ***P < 0.001 relative to DMSO (**c**) (one-way ANOVA followed by Dunnett's multiple comparisons test).

1088



1089

1090

1091

1092

Fig. 6: Proposed model for the roles of ErbBs in the regulation of SARS-CoV-2 infection and pathogenesis and the mechanism of action of pan-ErbB inhibitors.

1093

By inhibiting ErbB4, lapatinib suppresses SARS-CoV-2 entry. By inhibiting pan-ErbB activation by various ligands and unopposed Ang II effect, lapatinib inhibits activation of signaling pathways known to be activated and deleterious in severe pandemic coronaviral infections, thereby protecting from inflammation and tissue injury.

1095

1096

1097

1098

1099

1100

1101

1102

1103

1104

1105

1106

1107

1108

1109

1110

1111

1112

1113

1114 **Extended data**

1115

1116 **This document includes:**

1117 1. Extended data figures and figure legends

1118 2. Supplementary discussion

1119 3. Extended data references

1120

1121

1122

1123

1124

1125

1126

1127

1128

1129

1130

1131

1132

1133

1134

1135

1136

1137

1138

1139

1140

1141

1142

1143

1144

1145

1146

1147

1148

1149

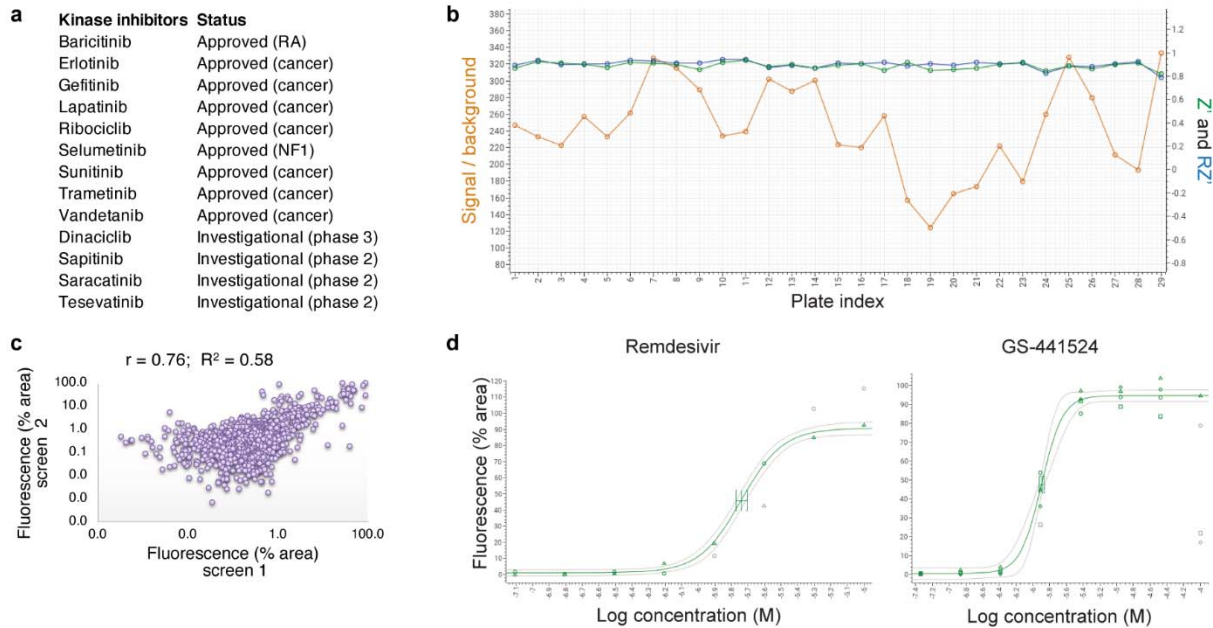
1150

1151

1152

1153

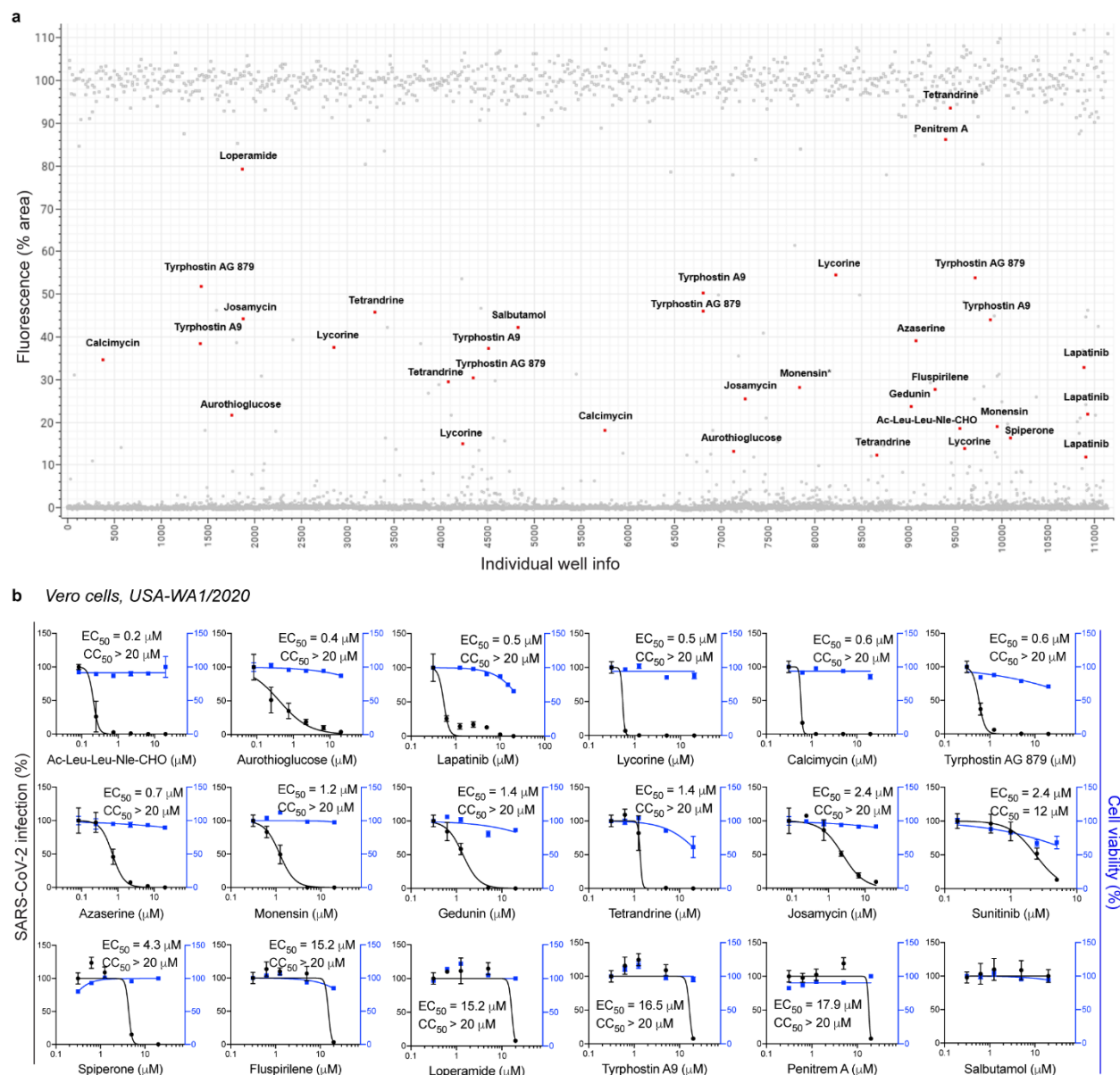
1154 **Extended data figures**



1155
1156
1157
1158
1159
1160
1161
1162
1163
1164
1165
1166
1167
1168

Extended data fig. 1: Characteristics and of the HTS.

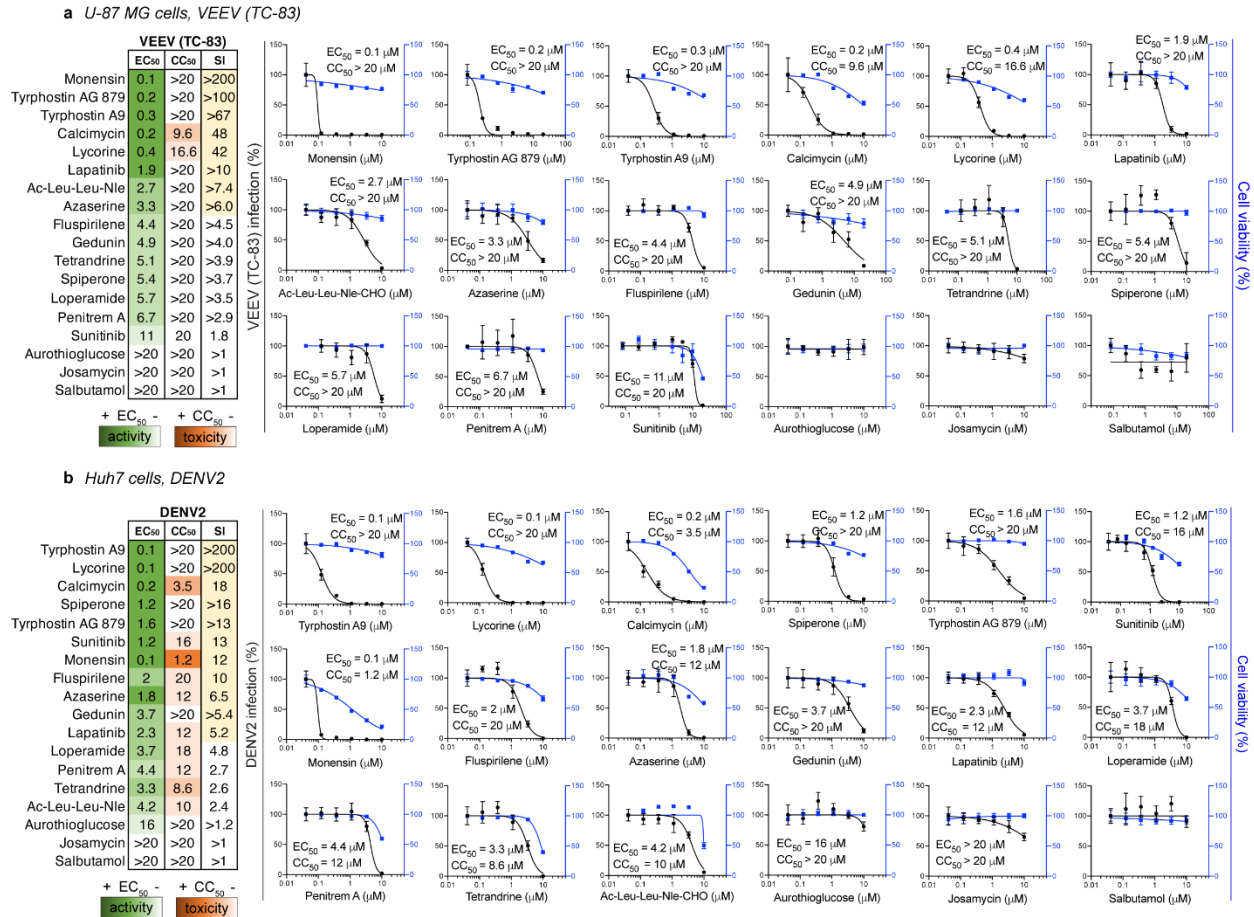
a, The kinase inhibitors included in the self-assembled set. **b**, Quality control of each individual plate of the 29 screened by determination of the signal-to-background (S/B), and the Z' and RZ' values. All three parameters were measured for each 384-well screening plate using the virus control (infected, DMSO treated) and cell control (uninfected, untreated) wells. S/B values ranged from 124 – 333. Z' and RZ' values were > 0.78. Generally, S/B values >10 and (R)Z' values >0,5 are accepted as qualitative assays. All parameters were calculated using Genedata Screener. **c**, Scatter plot of the two replicate screens with a Pearson's correlation coefficient (r) of 0.76. **d**, Dose-dependent rescue of Vero-eGFP cells from SARS-CoV-2-induced lethality by remdesivir and its major metabolite, GS-441524, used as positive controls, 4 days post-infection with SARS-CoV-2 (Belgium-GHB-03021, MOI=0.001)



1169
1170
1171
1172
1173
1174
1175
1176
1177
1178
1179
1180

Extended data fig. 2: Hits emerging from the HTS.

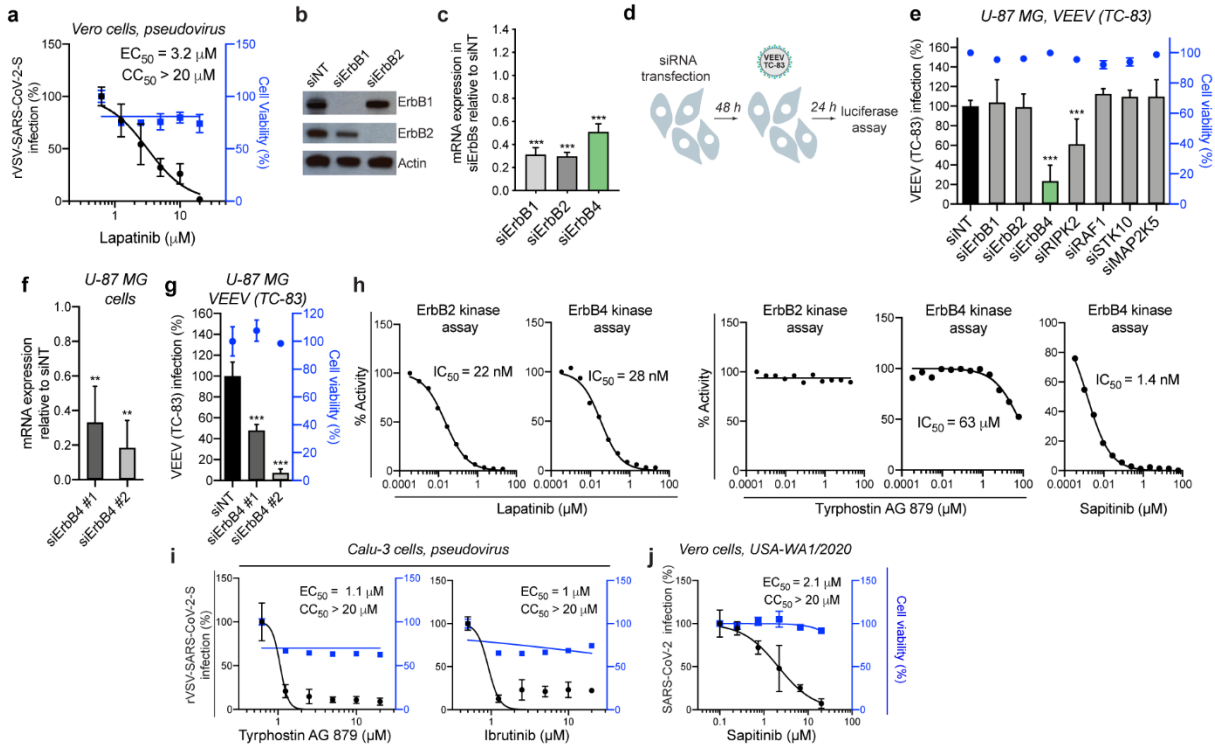
a, Percentage of fluorescence area values from all wells including the virus controls (infected, DMSO treated) and the cell controls (uninfected, untreated) from the 29 384-well plates. The red dots depict hits emerging in the screening. Grey dots represent reference compounds such as nelfinavir, GS-441524 and compounds not prioritized for further analysis. **b**, Dose response curves to the indicated hits emerging from the HTS of SARS-CoV-2 infection (black, USA-WA1/2020 strain, MOI=0.05) and cell viability (blue) in Vero cells measured via plaque and alamarBlue assays at 24 hours post-infection, respectively.



1181
 1182
 1183
 1184
 1185
 1186
 1187
 1188
 1189
 1190
 1191
 1192
 1193

Extended data fig. 3: Broad-spectrum potential of hits and kinase inhibitor set.

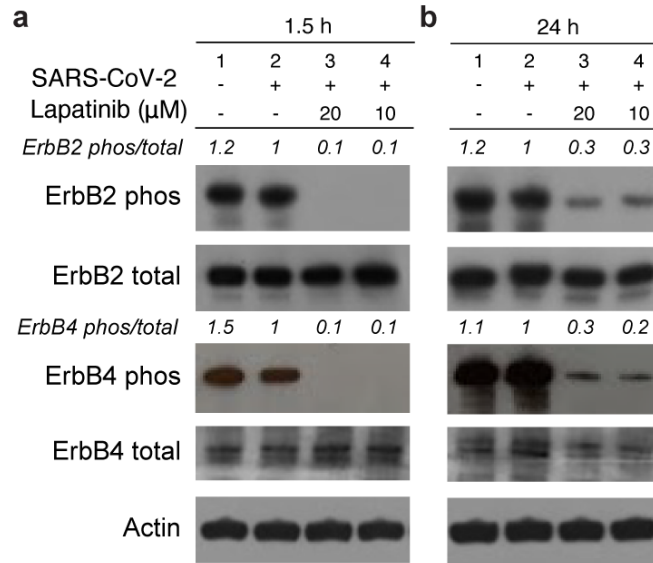
a, b, The 18 compounds emerging from the HTS were tested for their effect on VEEV (TC-83) (a) and DENV2 (b) infections in U-87 MG and Huh7 cells, respectively, measured via luciferase assays, and for their effect on cell viability measured via alamarBlue assays. Left panels: Heat maps of the EC₅₀ and CC₅₀ values of the indicated compounds color-coded based on the antiviral activity (green) and toxicity (orange). Selectivity indices (SI) greater than 5 are depicted in yellow. Right panels: Dose response curves to the indicated compounds of VEEV (TC-83) (MOI=0.1) or DENV2 (MOI=0.05) infections (black) in U-87 MG and Huh7 cells, respectively, measured via luciferase assays and cell viability (blue) measured by alamarBlue assays at 24 hours post-infection.



1194
1195
1196
1197
1198
1199
1200
1201
1202
1203
1204
1205
1206
1207
1208
1209
1210
1211
1212
1213
1214
1215
1216
1217
1218
1219
1220
1221

Extended data fig. 4: Validation of ErbB4 as an antiviral target.

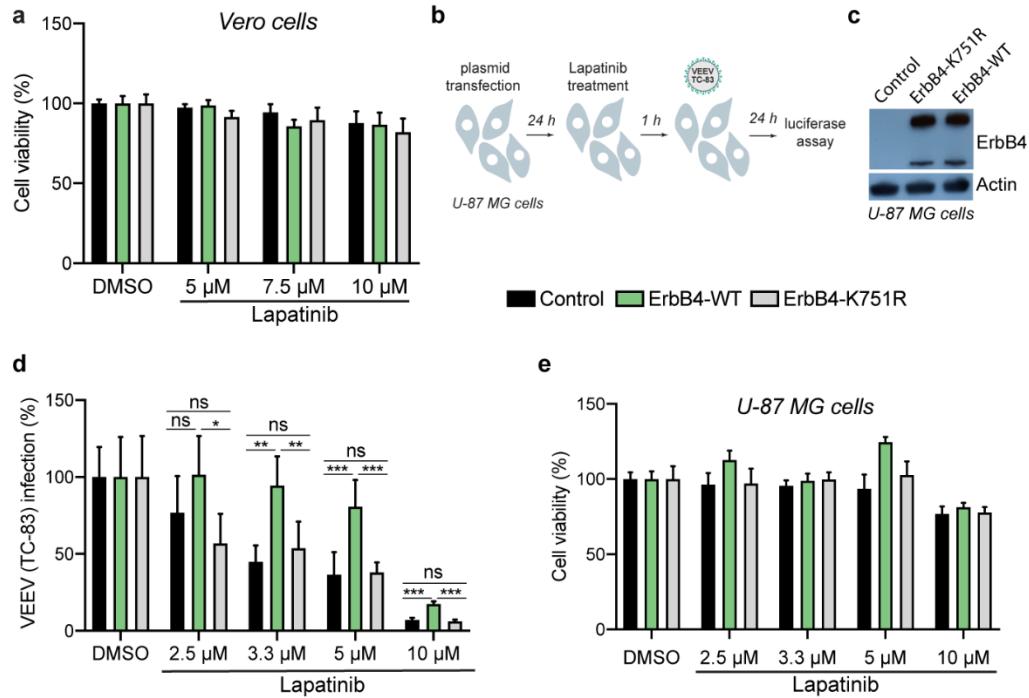
a, Dose response to lapatinib of rVSV-SARS-CoV-2-S infection (black) and cell viability (blue) in Vero cells measured via luciferase and alamarBlue assays at 24 hours post-infection with a standard inoculum, respectively. **b**, Confirmation of siRNA-mediated gene expression knockdown by Western blot in Vero cells at 48 hours after transfection. Notably, two anti-ErbB4 antibodies detected no signal of endogenous protein in Vero cells in two independent experiments. **c**, Confirmation of siRNA-mediated (ON-TARGETplus SMARTpool siRNAs (Dharmacon)) gene expression knockdown by RT-qPCR in Vero cells. Shown is gene expression normalized to GAPDH and expressed relative to the respective gene level in the non-target (siNT) control at 48 hours post-transfection. **d**, Schematic of the experiments shown in panels **e-g**. **e**, VEEV (T-83) infection by luciferase assays and cell viability by alamarBlue assays (blue) measured at 24 hours post-infection of U-87 MG cells transfected with the indicated siRNA pools (MOI=0.1). **f**, Confirmation of gene expression knockdown by RT-qPCR in U-87 MG cells at 48 hours post-transfection. **g**, VEEV (T-83) infection (MOI=0.1) measured by luciferase assays at 24 hours post-infection of U-87 MG cells transfected with the indicated siRNAs. Shown in blue is cell viability by alamarBlue assays. **h**, Dose response to lapatinib, tyrphostin AG 879 and sapatitinib of ErbB2 and/or ErbB4 kinase activity *in vitro* (Nanosyn). **i**, Dose response to tyrphostin AG 879 and ibrutinib of rVSV-SARS-CoV-2-S infection (black) by luciferase assays and cell viability (blue) by alamarBlue assays at 24 hours post-infection of Calu-3 cells. **j**, Dose response to sapatitinib of SARS-CoV-2 infection (black) by plaque assay and cell viability (blue) by alamarBlue assay 24 hours post-infection of Vero cells. Data in panels **a-g**, **i**, **j** are representative of 2 or more independent experiments. Individual experiments had 3 biological replicates, means \pm SD are shown. * $P < 0.01$, *** $P < 0.001$ relative to siNT by one-way ANOVA followed by Dunnett's multiple comparisons test.



1222
1223
1224
1225
1226
1227
1228
1229
1230
1231

Extended data fig. 5: Lapatinib treatment modulates ErbBs.

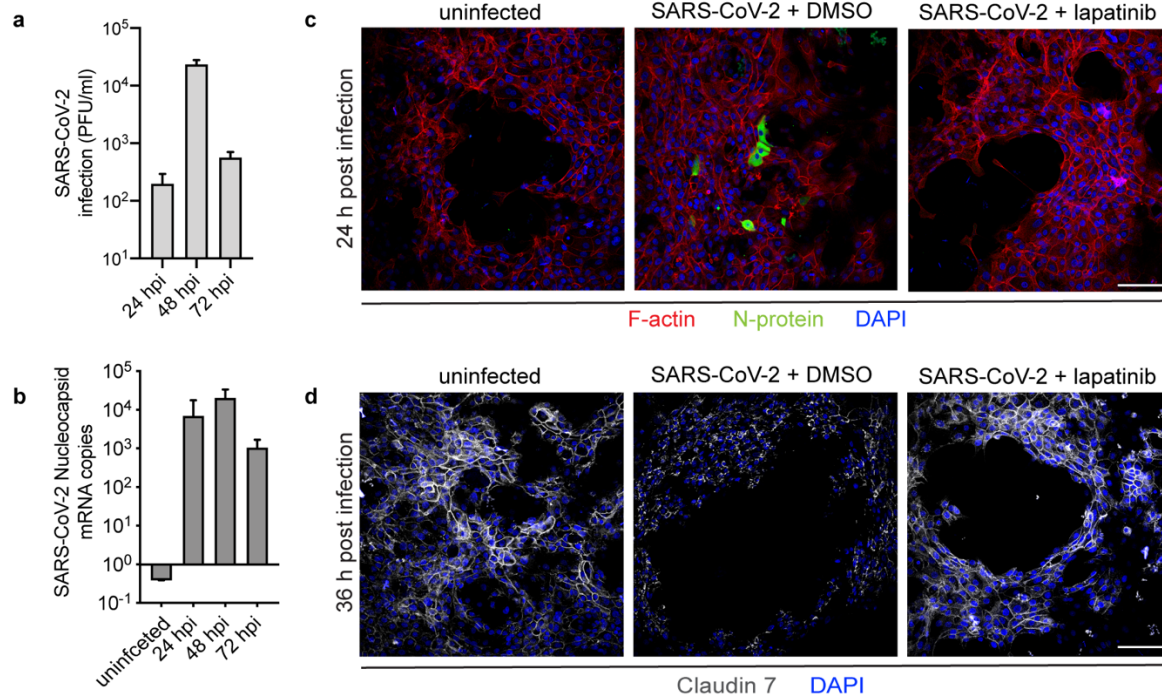
a, b, ErbB2 and ErbB4 phosphorylation in Calu-3 cells that are uninfected (lane 1), infected and treated with DMSO (lane 2) or infected and treated with lapatinib (lanes 3 and 4) measured by Western blotting 1.5 hours (**a**) and 24 hours (**b**) post-infection with SARS-CoV-2 (USA-WA1/2020 strain, MOI=1). Shown are representative membranes blotted for phospho- and total ErbB2, ErbB4, and actin and quantitative phospho- to total ErbB ratio data relative to infected cells treated with DMSO (lane 2).



1232
1233
1234
1235
1236
1237
1238
1239
1240
1241
1242
1243
1244
1245
1246

Extended data fig. 6: ErbB4 is a molecular target mediating lapatinib's antiviral effect.

a, Vero cell viability measured by alamarBlue assays 48 hours post-transfection of the indicated plasmids. Data relative to the respective DMSO controls are shown. **b**, Schematics of the experiments shown in **c-e**. **c**, Level of ErbB4 and actin expression measured by Western blot following transfection of U-87 MG cells with control or ErbB4-expressing plasmids. **d**, Rescue of VEEV (TC-83) infection in the presence of lapatinib upon ectopic expression of the indicated plasmids measured by luciferase assays 24 hours after infection. **e**, U-87 MG cell viability measured by alamarBlue assays 48 hours post-transfection of the indicated plasmids. Data relative to the respective DMSO controls are shown. Shown in panels **a**, **d**, **e** are means±SD of results of two combined experiments conducted each with three (**a**) or five (**d**, **e**) replicates. * $P < 0.05$, ** $P < 0.01$, *** $P < 0.001$ relative to DMSO by 1-way ANOVA with Tukey's multiple comparisons test at each lapatinib concentration. Ns, non-significant.



1247
1248
1249
1250
1251
1252
1253
1254
1255
1256
1257
1258
1259
1260
1261
1262
1263
1264
1265

Extended data fig. 7: Human ALOs for studying the antiviral and tissue protective effects of lapatinib.

a, b, Viral titer by plaque assays in culture supernatants (**a**) and viral nucleocapsid (N) copy number analyzed by RT-qPCR in lysates (**b**) from human lung organoids at 24, 48 and 72 hours post-infection. **c**, Confocal IF microscopy images of F-actin (red), SARS-CoV-2 nucleocapsid (green) and DAPI (blue) in naïve and SARS-CoV-2-infected ALOs pre-treated with DMSO or 10 μ M lapatinib 24 hours post-infection. **d**, Confocal IF microscopy images of Claudin 7 (grey) and DAPI (blue) in naïve or SARS-CoV-2- infected ALOs treated at 4 hours post-infection either with DMSO or 10 μ M lapatinib and imaged at 36 hours post-infection. Representative merged images at 20x magnification are shown in panels **c** and **d**. Scale bars are 100 μ m.

Supplementary discussion

Safety considerations and drug-drug interactions of lapatinib

Although toxicity is a concern when targeting host functions, lapatinib has a favorable safety profile, particularly when used as a monotherapy and for short durations, as those required to treat acute infections.

Notably, lapatinib's safety profile in the package insert was based on data from over 12,000 patients with advanced cancer who received lapatinib in combination with capecitabine or trastuzumab plus an aromatase inhibitor and for long durations¹⁻³. As monotherapy, lapatinib was tested in several open-label studies with a median duration of 7-28 weeks in patients with advanced cancer⁴⁻¹¹. The most common adverse events attributed to lapatinib were diarrhea, rash, nausea, pruritus, and fatigue, with diarrhea being the most common adverse event resulting in drug discontinuation. The most common laboratory abnormalities with combination therapy were increased liver function tests, which were infrequently severe^{1-3,12}. More severe adverse events including transient, reversible decreases in left ventricular ejection fraction, prolongation of QT interval, and hepatotoxicity, were also documented, yet infrequently, and with the exception of cardiac toxicity, primarily in patients receiving lapatinib in combination treatment^{1,10,13,14}.

Notably, unlike erlotinib and gefitinib, lapatinib monotherapy has not been associated with pneumonitis, interstitial lung disease or lung fibrosis⁴⁻¹¹. The estimated incidence of 0.2% for these adverse effects is based on patients receiving lapatinib in combination with other drugs¹⁵⁻²⁰ known to cause pneumonitis and/or lung fibrosis²¹⁻²³, and sometimes also with radiation, for a median duration of 24-45 weeks. We predict that lapatinib's distinct off-target profile accounts for this difference in the occurrence of these adverse events. Indeed, cyclin G-associated kinase (GAK), an off-target of erlotinib ($K_D=3.1$ nM, $IC_{50}=0.88$ μ M) and gefitinib ($K_D=6.5$ nM, $IC_{50}=0.41$ μ M), but not of lapatinib ($K_D=980$ nM, $IC_{50}>5$ μ M)²⁴, has been implicated in pulmonary alveolar function and stem cell regeneration, and its inhibition is thought to be the mechanism underlying gefitinib- and erlotinib- induced lung toxicity^{25,26}.

An important consideration with lapatinib is, however, its potential for drug-drug interactions. Since metabolized by CYP3A4, concurrent use of suppressors of CYP3A4 should be avoided to reduce risk of QT prolongation. Concurrent treatment with CYP3A4 inducers should also be avoided, as this can reduce lapatinib's levels to sub-therapeutic. Of particular relevance is the CYP3A4 inducer dexamethasone used as standard of care for moderate COVID-19 patients. Since other steroids do not induce CYP3A4, lapatinib could be studied in combination with hydrocortisone or prednisone, which have been shown to comparably protect COVID-19 patients²⁷⁻²⁹.

Other hits emerging in the screen

Another approved anticancer drug that emerged in the HTS was sunitinib, a multi-kinase inhibitor that we have shown to protect mice from DENV and EBOV challenges when given in combination with erlotinib by inhibiting NAK-mediated intracellular viral trafficking³⁰⁻³². Sunitinib was recently shown to suppress pan-corona pseudotyped viral infections³³. AG 879, another kinase inhibitor demonstrating anti-SARS-CoV-2 activity, was reported to suppress replication of multiple viruses including a mouse hepatitis virus (Coronaviridae) in cultured cells and to protect mice from influenza A virus (IAV) challenge³⁴⁻³⁶. Nevertheless, since we could not confirm its anti-ErbB activity, the precise target(s) mediating the antiviral effect remain to be elucidated.

Ion transport across cell membranes is another function that emerged in our HTS as a candidate target for anti-SARS-CoV-2 approaches. Among the hits was tetrandine, a calcium channel blocker with anti-inflammatory and anti-fibrogenic properties used as a medicinal herb for the treatment of lung silicosis, liver cirrhosis, and rheumatoid arthritis³⁷. Tetrandine was previously shown to inhibit EBOV entry in cultured cells and protect EBOV-infected mice by inhibiting endosomal calcium channels³⁸. Monensin, an antiprotozoal agent, and calcimycin, shown to inhibit VSV and IAV infections^{39,40}, are both ionophores that facilitate the transport of sodium/potassium and calcium across the membrane, respectively. Spiperone, an activator of chloride channels licensed in Japan for the treatment of schizophrenia, was another hit.

The emergence of gedunin, a natural product that inhibits HSP90 and has anti-inflammatory properties, suggests a potential role for HSP90 in SARS-CoV-2 infection, as in other viral infections^{41,42}. Lycorine, a protein synthesis inhibitor⁴³ was also shown to suppress replication of multiple viruses including SARS-CoV in cultured cells⁴⁴⁻⁴⁷ and mortality of mice infected with human enterovirus 71⁴⁸. The underlying mechanism of action in influenza was thought to be inhibition of export of viral ribonucleoprotein complexes from the nucleus⁴⁴, yet lycorine also exhibits anti-inflammatory effects⁴⁹. Azaserine is a natural serine derivative that irreversibly inhibits γ -glutamyltransferase in the metabolic hexosamine pathway. Independently of this target, it was shown to protect from endothelial cell inflammation and injury⁵⁰.

Aurothioglucose has been used for the treatment of rheumatoid arthritis and is thought to inhibit the activity of adenylyl cyclase in inflammatory pathways⁵¹. Ac-Leu-Leu-Nle-CHO is used as a research tool to inhibit calpain 1 and 2 (CAPN1 and 2)⁵², cysteine proteases required for SARS-CoV⁵³, echovirus 1⁵⁴ and herpes simplex virus⁵⁵ infections. Targeting calpain proteases was shown to inhibit SARS-CoV-2⁵⁶, SARS-CoV⁵⁷ and IAV replication⁵⁸ and to exert anti-inflammatory and tissue protective effects^{59,60} including in a reovirus-induced myocarditis mouse model⁶¹. Beyond their host-targeted effects, Ac-Leu-Leu-Nle-CHO and aurothioglucose may have direct antiviral effects against the SARS-CoV-2 M^{pro} or 3C-like proteases, respectively^{56,62}. Lastly, josamycin is a natural macrolide antibiotic with an anti-inflammatory activity used in humans in Europe and Japan. Other macrolides have shown anti-IAV and anti-inflammatory activities⁶³. These findings reveal candidate targets for anti-SARS-CoV-2 approaches. Moreover, they underscore the potential utility of natural products as broad-spectrum antivirals, yet limited scalability typically challenges the use of these products.

Extended data references

- 1 Novartis. Tykerb (U.S. package insert). (2018).
- 2 Pivot, X. *et al.* CEREBEL (EGF111438): A Phase III, Randomized, Open-Label Study of Lapatinib Plus Capecitabine Versus Trastuzumab Plus Capecitabine in Patients With Human Epidermal Growth Factor Receptor 2-Positive Metastatic Breast Cancer. *J Clin Oncol* **33**, 1564-1573, doi:10.1200/jco.2014.57.1794 (2015).
- 3 Schwartzberg, L. S. *et al.* Lapatinib plus letrozole as first-line therapy for HER-2+ hormone receptor-positive metastatic breast cancer. *The oncologist* **15**, 122-129, doi:10.1634/theoncologist.2009-0240 (2010).
- 4 Blackwell, K. L. *et al.* Single-agent lapatinib for HER2-overexpressing advanced or metastatic breast cancer that progressed on first- or second-line trastuzumab-containing regimens. *Ann Oncol* **20**, 1026-1031, doi:10.1093/annonc/mdn759 (2009).
- 5 Blackwell, K. L. *et al.* Randomized study of Lapatinib alone or in combination with trastuzumab in women with ErbB2-positive, trastuzumab-refractory metastatic breast cancer. *J Clin Oncol* **28**, 1124-1130, doi:10.1200/jco.2008.21.4437 (2010).
- 6 Burris, H. A., 3rd *et al.* Phase I safety, pharmacokinetics, and clinical activity study of lapatinib (GW572016), a reversible dual inhibitor of epidermal growth factor receptor tyrosine kinases, in heavily pretreated patients with metastatic carcinomas. *J Clin Oncol* **23**, 5305-5313, doi:10.1200/jco.2005.16.584 (2005).
- 7 Burstein, H. J. *et al.* A phase II study of lapatinib monotherapy in chemotherapy-refractory HER2-positive and HER2-negative advanced or metastatic breast cancer. *Ann Oncol* **19**, 1068-1074, doi:10.1093/annonc/mdm601 (2008).
- 8 Gomez, H. L. *et al.* Efficacy and Safety of Lapatinib As First-Line Therapy for ErbB2-Amplified Locally Advanced or Metastatic Breast Cancer. *Journal of Clinical Oncology* **26**, 2999-3005, doi:10.1200/jco.2007.14.0590 (2008).
- 9 Hurvitz, S. A. & Kakkar, R. Role of lapatinib alone or in combination in the treatment of HER2-positive breast cancer. *Breast Cancer (Dove Med Press)* **4**, 35-51, doi:10.2147/BCTT.S29996 (2012).
- 10 Perez, E. A. *et al.* Cardiac safety of lapatinib: pooled analysis of 3689 patients enrolled in clinical trials. *Mayo Clinic proceedings* **83**, 679-686, doi:10.4065/83.6.679 (2008).
- 11 Toi, M. *et al.* Lapatinib monotherapy in patients with relapsed, advanced, or metastatic breast cancer: efficacy, safety, and biomarker results from Japanese patients phase II studies. *British journal of cancer* **101**, 1676-1682, doi:10.1038/sj.bjc.6605343 (2009).
- 12 Piccart-Gebhart, M. *et al.* Adjuvant Lapatinib and Trastuzumab for Early Human Epidermal Growth Factor Receptor 2-Positive Breast Cancer: Results From the

- Randomized Phase III Adjuvant Lapatinib and/or Trastuzumab Treatment Optimization Trial. *J Clin Oncol* **34**, 1034-1042, doi:10.1200/jco.2015.62.1797 (2016).
- 13 Kloth, J. S. L. *et al.* Incidence and relevance of QTc-interval prolongation caused by tyrosine kinase inhibitors. *British journal of cancer* **112**, 1011-1016, doi:10.1038/bjc.2015.82 (2015).
 - 14 Dogan, E. *et al.* Evaluation of cardiac safety of lapatinib therapy for ErbB2-positive metastatic breast cancer: a single center experience. *Medical oncology (Northwood, London, England)* **29**, 3232-3239, doi:10.1007/s12032-012-0253-5 (2012).
 - 15 Hackshaw, M. D. *et al.* Incidence of pneumonitis/interstitial lung disease induced by HER2-targeting therapy for HER2-positive metastatic breast cancer. *Breast cancer research and treatment* **183**, 23-39, doi:10.1007/s10549-020-05754-8 (2020).
 - 16 Jagiello-Gruszfeld, A. *et al.* A single-arm phase II trial of first-line paclitaxel in combination with lapatinib in HER2-overexpressing metastatic breast cancer. *Oncology* **79**, 129-135, doi:10.1159/000318043 (2010).
 - 17 Capri, G. *et al.* An open-label expanded access study of lapatinib and capecitabine in patients with HER2-overexpressing locally advanced or metastatic breast cancer. *Ann Oncol* **21**, 474-480, doi:10.1093/annonc/mdp373 (2010).
 - 18 Xu, B.-H. *et al.* Lapatinib plus capecitabine in treating HER2-positive advanced breast cancer: efficacy, safety, and biomarker results from Chinese patients. *Chin J Cancer* **30**, 327-335, doi:10.5732/cjc.010.10507 (2011).
 - 19 Bates, C. A. *et al.*
 - 20 Brenner, T. *et al.* Rapid-Onset Acute Respiratory Distress Syndrome (ARDS) in a Patient Undergoing Metastatic Liver Resection: A Case Report and Review of the Literature. *Anesthesiol Res Pract* **2010**, 586425, doi:10.1155/2010/586425 (2010).
 - 21 Chan, A. K., Choo, B. A. & Glaholm, J. Pulmonary toxicity with oxaliplatin and capecitabine/5-Fluorouracil chemotherapy: a case report and review of the literature. *Onkologie* **34**, 443-446, doi:10.1159/000331133 (2011).
 - 22 Torrisi, J. M. *et al.* CT findings of chemotherapy-induced toxicity: what radiologists need to know about the clinical and radiologic manifestations of chemotherapy toxicity. *Radiology* **258**, 41-56, doi:10.1148/radiol.10092129 (2011).
 - 23 Bielopolski, D. *et al.* Paclitaxel-induced pneumonitis in patients with breast cancer: case series and review of the literature. *Journal of chemotherapy (Florence, Italy)* **29**, 113-117, doi:10.1179/1973947815y.0000000029 (2017).
 - 24 Asquith, C. R. M. *et al.* Design and Analysis of the 4-Anilinoquin(az)oline Kinase Inhibition Profiles of GAK/SLK/STK10 Using Quantitative Structure-Activity Relationships. *ChemMedChem* **15**, 26-49, doi:10.1002/cmdc.201900521 (2020).

- 25 Tabara, H. *et al.* Neonatal lethality in knockout mice expressing the kinase-dead form of the gefitinib target GAK is caused by pulmonary dysfunction. *PLoS One* **6**, e26034, doi:10.1371/journal.pone.0026034 (2011).
- 26 Bates, C. A. *et al.* in *A61. EPITHELIAL BIOLOGY American Thoracic Society International Conference Abstracts* A2125-A2125 (American Thoracic Society, 2019).
- 27 Group, T. W. R. E. A. f. C.-T. W. Association Between Administration of Systemic Corticosteroids and Mortality Among Critically Ill Patients With COVID-19: A Meta-analysis. *JAMA* **324**, 1330-1341, doi:10.1001/jama.2020.17023 (2020).
- 28 Dequin, P.-F. *et al.* Effect of Hydrocortisone on 21-Day Mortality or Respiratory Support Among Critically Ill Patients With COVID-19: A Randomized Clinical Trial. *JAMA* **324**, 1298-1306, doi:10.1001/jama.2020.16761 (2020).
- 29 Investigators, T. W. C. f. t. R.-C. Effect of Hydrocortisone on Mortality and Organ Support in Patients With Severe COVID-19: The REMAP-CAP COVID-19 Corticosteroid Domain Randomized Clinical Trial. *JAMA* **324**, 1317-1329, doi:10.1001/jama.2020.17022 (2020).
- 30 Neveu, G. *et al.* Identification and Targeting of an Interaction between a Tyrosine Motif within Hepatitis C Virus Core Protein and AP2M1 Essential for Viral Assembly. *PLoS pathogens* **8**, e1002845 (2012).
- 31 Bekerman, E. *et al.* Anticancer kinase inhibitors impair intracellular viral trafficking and exert broad-spectrum antiviral effects. *The Journal of clinical investigation* **127**, doi:10.1172/JCI89857 (2017).
- 32 Pu, S. *et al.* BIKE regulates dengue virus infection and is a cellular target for broad-spectrum antivirals. *Antiviral Res* **184**, 104966, doi:10.1016/j.antiviral.2020.104966 (2020).
- 33 Wang, P.-G., Tang, D.-J., Hua, Z., Wang, Z. & An, J. Sunitinib reduces the infection of SARS-CoV, MERS-CoV and SARS-CoV-2 partially by inhibiting AP2M1 phosphorylation. *Cell Discovery* **6**, 71, doi:10.1038/s41421-020-00217-2 (2020).
- 34 Kumar, N., Liang, Y., Parslow, T. G. & Liang, Y. Receptor Tyrosine Kinase Inhibitors Block Multiple Steps of Influenza A Virus Replication. *Journal of virology* **85**, 2818-2827, doi:10.1128/jvi.01969-10 (2011).
- 35 Kumar, N., Sharma, N. R., Ly, H., Parslow, T. G. & Liang, Y. Receptor tyrosine kinase inhibitors that block replication of influenza a and other viruses. *Antimicrobial agents and chemotherapy* **55**, 5553-5559, doi:10.1128/AAC.00725-11 (2011).
- 36 Zoeller, R. A. & Geoghegan-Barek, K. A cell-based high-throughput screen identifies tyrphostin AG 879 as an inhibitor of animal cell phospholipid and fatty acid biosynthesis. *Biochemistry and Biophysics Reports* **18**, 100621, doi:<https://doi.org/10.1016/j.bbrep.2019.100621> (2019).

- 37 Kwan, C. Y. & Achike, F. I. Tetrandrine and related bis-benzylisoquinoline alkaloids from medicinal herbs: cardiovascular effects and mechanisms of action. *Acta pharmacologica Sinica* **23**, 1057-1068 (2002).
- 38 Sakurai, Y. *et al.* Ebola virus. Two-pore channels control Ebola virus host cell entry and are drug targets for disease treatment. *Science* **347**, 995-998, doi:10.1126/science.1258758 (2015).
- 39 Onishi, E., Natori, K. & Yamazaki, S. The antiviral effect of phorbol ester and calcium ionophore A23187 is not mediated by interferons. *Journal of interferon research* **11**, 171-175, doi:10.1089/jir.1991.11.171 (1991).
- 40 Marois, I. *et al.* Inhibition of Influenza Virus Replication by Targeting Broad Host Cell Pathways. *PLOS ONE* **9**, e110631, doi:10.1371/journal.pone.0110631 (2014).
- 41 Geller, R., Taguwa, S. & Frydman, J. Broad action of Hsp90 as a host chaperone required for viral replication. *Biochimica et biophysica acta* **1823**, 698-706, doi:10.1016/j.bbamcr.2011.11.007 (2012).
- 42 Amraiz D, Z. N., Fatima M. Antiviral evaluation of an Hsp90 inhibitor, gedunin, against dengue virus. *Trop J Pharm Res* **16**, 997-1004 (2017).
- 43 Vrijsen, R., Vanden Berghe, D. A., Vlietinck, A. J. & Boeyé, A. Lycorine: a eukaryotic termination inhibitor? *The Journal of biological chemistry* **261**, 505-507 (1986).
- 44 Yang, L. *et al.* Tandem mass tag-based quantitative proteomic analysis of lycorine treatment in highly pathogenic avian influenza H5N1 virus infection. *PeerJ* **7**, e7697-e7697, doi:10.7717/peerj.7697 (2019).
- 45 Ieven, M., van den Berghe, D. A. & Vlietinck, A. J. Plant antiviral agents. IV. Influence of lycorine on growth pattern of three animal viruses. *Planta medica* **49**, 109-114 (1983).
- 46 Szlávik, L. *et al.* Alkaloids from *Leucojum vernum* and antiretroviral activity of Amaryllidaceae alkaloids. *Planta medica* **70**, 871-873, doi:10.1055/s-2004-827239 (2004).
- 47 Li, S. Y. *et al.* Identification of natural compounds with antiviral activities against SARS-associated coronavirus. *Antiviral Res* **67**, 18-23, doi:10.1016/j.antiviral.2005.02.007 (2005).
- 48 Liu, J. *et al.* Lycorine reduces mortality of human enterovirus 71-infected mice by inhibiting virus replication. *Virology journal* **8**, 483, doi:10.1186/1743-422x-8-483 (2011).
- 49 Li, S., Liu, X., Chen, X. & Bi, L. Research Progress on Anti-Inflammatory Effects and Mechanisms of Alkaloids from Chinese Medical Herbs. *Evidence-Based Complementary and Alternative Medicine* **2020**, 1303524, doi:10.1155/2020/1303524 (2020).
- 50 Rajapakse, A. G., Ming, X. F., Carvas, J. M. & Yang, Z. The hexosamine biosynthesis inhibitor azaserine prevents endothelial inflammation and dysfunction under hyperglycemic condition through antioxidant effects. *American journal of physiology*.

- Heart and circulatory physiology* **296**, H815-822, doi:10.1152/ajpheart.00756.2008 (2009).
- 51 Botz, B. *et al.* Differential regulatory role of pituitary adenylate cyclase-activating polypeptide in the serum-transfer arthritis model. *Arthritis & rheumatology (Hoboken, N.J.)* **66**, 2739-2750, doi:10.1002/art.38772 (2014).
- 52 Sasaki, T. *et al.* Inhibitory effect of di- and tripeptidyl aldehydes on calpains and cathepsins. *Journal of enzyme inhibition* **3**, 195-201, doi:10.3109/14756369009035837 (1990).
- 53 Schneider, M. *et al.* Severe acute respiratory syndrome coronavirus replication is severely impaired by MG132 due to proteasome-independent inhibition of M-calpain. *J Virol* **86**, 10112-10122, doi:10.1128/jvi.01001-12 (2012).
- 54 Upla, P. *et al.* Calpain 1 and 2 are required for RNA replication of echovirus 1. *J Virol* **82**, 1581-1590, doi:10.1128/jvi.01375-07 (2008).
- 55 Zheng, K. *et al.* Calcium-signal facilitates herpes simplex virus type 1 nuclear transport through slingshot 1 and calpain-1 activation. *Virus research* **188**, 32-37, doi:10.1016/j.virusres.2014.03.016 (2014).
- 56 Ma, C. *et al.* Boceprevir, GC-376, and calpain inhibitors II, XII inhibit SARS-CoV-2 viral replication by targeting the viral main protease. *Cell research* **30**, 678-692, doi:10.1038/s41422-020-0356-z (2020).
- 57 Barnard, D. L. *et al.* Inhibition of severe acute respiratory syndrome-associated coronavirus (SARSCoV) by calpain inhibitors and beta-D-N4-hydroxycytidine. *Antiviral chemistry & chemotherapy* **15**, 15-22, doi:10.1177/095632020401500102 (2004).
- 58 Blanc, F. *et al.* Targeting host calpain proteases decreases influenza A virus infection. *American journal of physiology. Lung cellular and molecular physiology* **310**, L689-699, doi:10.1152/ajplung.00314.2015 (2016).
- 59 Li, X. *et al.* Over-expression of calpastatin inhibits calpain activation and attenuates myocardial dysfunction during endotoxaemia. *Cardiovascular research* **83**, 72-79, doi:10.1093/cvr/cvp100 (2009).
- 60 Supinski, G. S. & Callahan, L. A. Calpain activation contributes to endotoxin-induced diaphragmatic dysfunction. *American journal of respiratory cell and molecular biology* **42**, 80-87, doi:10.1165/rcmb.2008-0275OC (2010).
- 61 DeBiasi, R. L., Edelstein, C. L., Sherry, B. & Tyler, K. L. Calpain inhibition protects against virus-induced apoptotic myocardial injury. *J Virol* **75**, 351-361, doi:10.1128/jvi.75.1.351-361.2001 (2001).
- 62 Baker, J. D., Uhrich, R. L., Kraemer, G. C., Love, J. E. & Kraemer, B. C. A drug repurposing screen identifies hepatitis C antivirals as inhibitors of the SARS-CoV2 main protease. *PLOS ONE* **16**, e0245962, doi:10.1371/journal.pone.0245962 (2021).

- 63 Sugamata, R. *et al.* Leucomycin A3, a 16-membered macrolide antibiotic, inhibits influenza A virus infection and disease progression. *The Journal of antibiotics* **67**, 213-222, doi:10.1038/ja.2013.132 (2014).